

# First Principles, Explicit Interface Studies of Oxygen Vacancy and Chloride in Alumina Films for Corrosion Applications

Kevin Leung\*

*Sandia National Laboratories, MS 1415,*

*Albuquerque, NM 87185*

\*kleung@sandia.gov

(Dated: November 10, 2021)

## Abstract

Pitting corrosion is a much-studied and technologically relevant subject. However, the fundamental mechanisms responsible for the breakdown of the passivating oxide layer are still subjects of debate. Chloride anions are known to accelerate corrosion; relevant hypotheses include Cl insertion into positively charged oxygen vacancies in the oxide film, and Cl adsorption on passivating oxide surfaces, substituting for surface hydroxyl groups. In this work, we conduct large-scale first principles modeling of explicit metal/ $\text{Al}_2\text{O}_3$  interfaces to investigate the energetics and electronic structures associated with these hypotheses. The explicit interface models allow electron transfer that mimics electrochemical events, and the establishment of the relation between atomic structures at different interfaces and the electronic band alignment. For multiple model interfaces, we find that doubly charged oxygen vacancies, which are key ingredients of the point defect model (PDM) often used to analyze corrosion data, can only occur in the presence of a potential gradient that raises the voltage.  $\text{Cl}^-$  insertion into oxide films can be energetically favorable in some oxygen vacancy sites, depending on the voltage. We also discuss the challenges associated with explicit DFT modeling of these complex interfaces.

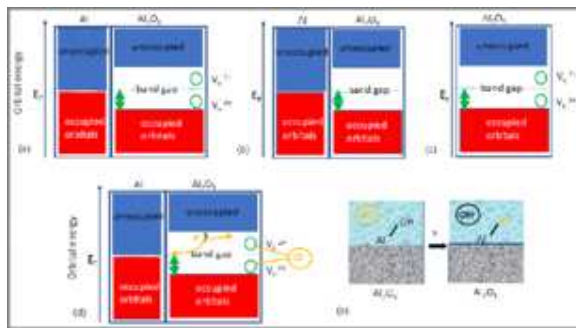


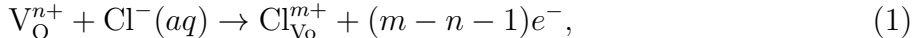
FIG. 1: Schematics of key science questions addressed. (a) The net charge in  $V_O$  depends on the energy level of the defect orbital relative to  $E_F$ . This can be computed in two steps: (b) no vacancy and then (c) no interface. If there is a electric field in the oxide film and/or a net charge transfer in the electrode, however, (a) must be used. (d)  $Cl^-$  insertion into oxygen vacancies. (e)  $Cl^-$  substitution for a  $OH^-$  surface group.

## I. INTRODUCTION

Corrosion is known to cost billions to industry per year.<sup>1</sup> Extensive field work and bench-top experiments have been devoted to understanding and mitigating corrosion effects. Despite this, aspects of the fundamental mechanisms responsible for pitting corrosion, which involves localized breakdown of passivating oxides on metal surfaces, remain debated.

In this work, we apply Density Functional Theory (DFT) calculations to investigate the defect electronic structure and the energetics of oxygen vacancies and  $Cl^-$  anions in model oxide films in direct contact with aluminum metal. These oxide films are known to be a few nanometers thick.<sup>2</sup> Our models are geared towards atmospheric corrosion conditions but our predictions are also relevant to aluminum immersed in aqueous electrolytes. We adopt computationally costly DFT models with explicit metal/oxide interfaces to allow electron transfer between defects in the passivating oxide film and the metal. This allows us to mimic electrochemical (electron transfer) events and generate finite electric fields in the oxide. Both will be shown to be crucial for making connections to continuum models which have been used to analyze corrosion.<sup>3,4</sup> We focus on two hypotheses postulated in the literature related to pitting initiation via breakdown in alumina surface films. One revolves around the key role of positively charged oxygen vacancies ( $V_O$ ). The other, which we touch on more briefly, concerns  $Cl^-$  substitution of surface  $OH^-$  groups. See Fig. 1.

Positively charged  $V_O$  are key ingredients of the point defect model (PDM)<sup>3-9</sup> widely used to analyze time-dependent corrosion behavior.  $Cl^-$  is an impurity well-known to accelerate pitting corrosion in many metals.<sup>10-16</sup>  $Cl^-$  is more detrimental than other halide anions.<sup>5</sup>  $Cl^-$  insertion into  $V_O^{2+}$  has been suggested to play a main role in corrosion via a  $Cl^-$  insertion reaction:<sup>4</sup>



where “(aq)” denotes aqueous phase. The electron ( $e^-$ ) released indicates that Eq. 1 is electrochemical in nature, and is therefore voltage-dependent. Indeed, in benchtop experiments, applying voltages above a threshold is linked to the onset of pitting corrosion.<sup>17,18</sup> In aluminum metal immersed in aqueous electrolytes, the threshold appears to be at  $\Phi_{ext} > -0.5$  V vs. standard hydrogen electrode (SHE), depending on the salt concentration and pH.<sup>19,20</sup>  $Cl^-$  implantation and other experiments have been performed to interrogate this hypothesis.<sup>21-23</sup>

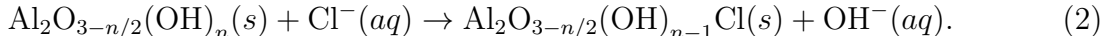
To model  $e^-$  transfer effects on corrosion requires a quantum mechanical treatment of valence  $e^-$ , with DFT being a standard compromise between accuracy and computational cost. Our first step is to apply DFT models with explicit Al|Al<sub>2</sub>O<sub>3</sub> interfaces to investigate the net charge in oxygen vacancies, and examine under what conditions  $V_O^{2+}$  ( $n=2$ ) exists. Fig. 1 illustrates this key issue: the net charges of defects like O-vacancies cannot be manually assigned, but are determined by the the vacancy orbital energy level relative to the Fermi level ( $E_F$ ).

Previous DFT work that has studied the Al metal/Al<sub>2</sub>O<sub>3</sub> interface<sup>24-37</sup> has not simultaneously considered defects like oxygen vacancies. While oxygen vacancies in Al<sub>2</sub>O<sub>3</sub> have been examined using DFT,<sup>38-43</sup> most such calculations are conducted in the absence of metallic Al, which defines the Fermi level ( $E_F$ ), in the simulation cell.  $E_F$  is not well defined in insulators like Al<sub>2</sub>O<sub>3</sub> without a metal electrode because  $E_F$  should be pinned at  $p$ - or  $n$ -type defects seldom explicitly depicted in DFT simulation cells. As such,  $E_F$  has generally been treated as a free parameter. Furthermore, oxides modeled using periodic boundary conditions in all three spatial dimensions cannot support an electric field – unless the Berry’s phase approach is used.<sup>44</sup> Therefore oxide calculations in the absence of an metal electrode and an explicit metal/oxide interface assume a zero-field, “flat-band” approximation.<sup>45</sup> In addition, at metal/oxide interfaces, a contact potential at the metal/oxide interface exists; its value can be up to 2-3 V,<sup>37,46,47</sup> and its effect can only be captured if an explicit metal/oxide interface exists in the simulation cell. Finally, there are at least two interfaces, namely

metal/oxide and oxide/electrolyte (Fig. 1). These interfaces both contribute to the overall voltage measured in experiments, but how these interfacial structures separately affect the electronic band alignment is not well established.

Here we adopt simulation cells with both an explicit Al|Al<sub>2</sub>O<sub>3</sub> interface and an explicit V<sub>O</sub>. Using several interface models, we show that uncharged V<sub>O</sub> in the oxide film is most likely the norm under flat-band conditions; V<sub>O</sub><sup>2+</sup> are found to occur only in the presence of electric fields in the oxide film. In other words, aluminum metal shows less tendency to support V<sub>O</sub><sup>2+</sup> in the oxide film than expected, likely because it is among the more electronegative metals. Indeed, previous DFT modeling of amorphous Al<sub>2</sub>O<sub>3</sub> has suggested overall negative charging due to multiple defects.<sup>48,49</sup> We also investigate the energetics of Cl<sup>-</sup> insertion into V<sub>O</sub> and V<sub>O</sub><sup>2+</sup> (Fig. 1d), and show that insertion is favorable under certain conditions. Our work arguably represents an important step towards parameterization of the PDM model using first principles predictions. Note that one of the few DFT studies with both explicit metal/oxide interfaces and vacancies concerns Cr<sub>2</sub>O<sub>3</sub> and CrOOH at Cr interfaces. The authors there assume that the O-vacancies created are doubly positively charged, but do not confirm it. We propose that their V<sub>O</sub> charge assignment may need to be re-examined.<sup>50</sup>

For completeness, we also examine another main hypothesis of aluminum oxide film depassivation which concerns Cl<sup>-</sup> substituting for OH<sup>-</sup> on Al<sub>2</sub>O<sub>3</sub> surfaces (Fig. 1e). Specifically,



X-ray Photoemission Spectroscopy (XPS) measurements supported by DFT calculations of core electron spectra have made a convincing case that this substitution, without electron transfer, takes place on oxide-passivated Al metal surfaces.<sup>51-54</sup> Computationally, fluorination of AlOH groups using HF gas has been predicted to be energetically favorable.<sup>55</sup> Cl<sup>-</sup> substitution for surface OH<sup>-</sup> and insertion into oxide films have also been examined using DFT methods in Al<sub>2</sub>O<sub>3</sub>,<sup>56</sup> NiO,<sup>57</sup> α-Cr<sub>2</sub>O<sub>3</sub>,<sup>58,59</sup> α-Fe<sub>2</sub>O<sub>3</sub>,<sup>60,61</sup> and other oxides. However, Eq. 2 appears at odds with geochemistry research showing that Cl<sup>-</sup> is less effective than other anions like SO<sub>4</sub><sup>2-</sup> to cause dissolution of aluminum oxy-hydroxide.<sup>62-64</sup> In this work, we report DFT energetics associated with Cl<sup>-</sup> → OH<sup>-</sup> on the α-Al<sub>2</sub>O<sub>3</sub> (0001) surface using parameters consistent with those we apply to examine Cl<sup>-</sup> insertion into V<sub>O</sub> inside the oxide film, so that a comparison of mechanisms can be made.

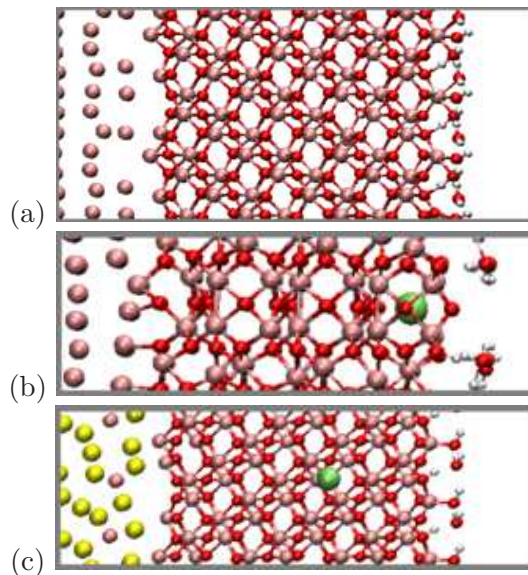


FIG. 2: Interfacial systems considered in this work. (a)  $\alpha$ - $\text{Al}_2\text{O}_3$  (0001) on Al(111); (b)  $\alpha$ - $\text{Al}_2\text{O}_3$  with grain boundary on Al(111); (c)  $\alpha$ - $\text{Al}_2\text{O}_3$  (0001) on Au(111). Pink, yellow, red, white, and green represent Al, Au, O, and H atoms, respectively.  $\text{Cl}^-$  insertion are shown in two cases. The  $+z$  direction points from the metal towards the oxide.

The passivating alumina films on Al metal surfaces are known to be amorphous.<sup>65</sup> We apply  $\alpha$ - $\text{Al}_2\text{O}_3$  as a model for the oxide film because it has interfaces which are better characterized; much of the DFT work in the has literature also adopted  $\alpha$ - $\text{Al}_2\text{O}_3$ . Grain boundaries in  $\alpha$ - $\text{Al}_2\text{O}_3$ , which may be better local approximations of amorphous oxides, are also considered. Our models and DFT calculations focus on atmospheric corrosion relevant to electronics bond wire degradation,<sup>66</sup> where Al metal, Au, and Al-Al intermetallics are all present. Despite this, we draw on perspectives, concepts, and pitting onset voltage dependences developed for Al corrosion in aqueous environments.

This work focuses on the solid interface and defect aspects. We will show that quantitative comparison of predicted voltages with experimental measurements may require future accurate treatment of the aqueous electrolyte. Other calculations in the literature relevant to corrosion deal with DFT screening of organic coating molecules<sup>67,68</sup> and MD simulations of water- and  $\text{Cl}^-$  adsorption surface sites in aqueous environments.<sup>69-73</sup> In the future, these elements can be added to explicit metal/oxide interface modeling, either in the same simulation cells or indirectly, via parameter passing protocols.

metal	oxide	gb	dimensions	stoichiometry	$k$ -sampling	Figure
Al(111)	$\alpha$ (001)	no	$4.81 \times 8.33 \times 52.00$	$(\text{Al}_{34})\text{Al}_{36}\text{O}_{54}(\text{H}_2\text{O})_6$	$3 \times 2 \times 1$	Fig. 2a
Al(111)	$\alpha$ (001)	no	$14.43 \times 16.663 \times 50.00$	$(\text{Al}_{204})\text{Al}_{216}\text{O}_{324}(\text{H}_2\text{O})_{36}$	$2 \times 2 \times 1$	Fig. 2a
Al(111)	$\alpha$	yes	$14.42 \times 26.87 \times 40.00$	$(\text{Al}_{216})\text{Al}_{264}\text{O}_{420}(\text{H}_2\text{O})_{24}$	$2 \times 1 \times 1$	Fig. 2b
Au(111)	$\alpha$ (001)	no	$14.43 \times 16.66 \times 50.00$	$(\text{Au}_{180}\text{Al}_{24})\text{Al}_{216}\text{O}_{324}(\text{H}_2\text{O})_{24}$	$2 \times 2 \times 1$	Fig. 2c
none	$\alpha$ (bulk)	no	$14.43 \times 12.45 \times 13.08$	$\text{Al}_{108}\text{O}_{162}$	$2 \times 2 \times 2$	NA
none	$\alpha$ (bulk)	no	$9.58 \times 8.30 \times 13.08$	$\text{Al}_{48}\text{O}_{72}$	$2 \times 2 \times 2$	NA

TABLE I: Computational details of representative, baseline simulation cells. The larger of the two “Fig. 2a” cell is used when inserting a  $V_{\text{O}}$ . Simulation cells which are  $2 \times 1$  and  $2 \times 2$  expansions in the lateral dimensions are also considered. Dimensions are in units of  $\text{\AA}^3$ . Brackets separate the metal and water zones from the oxide region. All oxide films are stoichiometric  $\text{Al}_2\text{O}_3$ , and initially, before selective deprotonation, integer numbers of  $\text{H}_2\text{O}$  molecules are added. There are excess number of metal atoms at the interface, so the metal zone contains non-integer number of metal layers.

## II. METHOD AND MODELS

### A. DFT Details

Most DFT calculations in this work are conducted under  $T=0$  K ultra-high vacuum (UHV) condition, using periodically replicated simulation cells and the Vienna Atomic Simulation Package (VASP) version 5.4.<sup>74-77</sup> A 400 eV planewave energy cutoff and a  $10^{-4}$  eV convergence criterion are enforced. Most calculations apply the PBE functional.<sup>78</sup> In some cases, HSE06 is used for spot check.<sup>79-81</sup> Spin-polarization is turned off because a net spin is found to only accumulate in the metallic region, and it barely affects the total energy.

Representative, baseline simulation cells are listed in Table I. The models with explicit interfaces are depicted in Fig. 2; they contain a vacuum region on top (in the  $+z$  direction), and a Al(111) metal slab at the bottom, with the bottom-most layer of metal atoms kept frozen. We also consider an Au(111) example (Fig. 2c), because Au is present in microelectronics bond pads,<sup>66</sup> and because it represents a metal with a higher work function and an interesting comparison with Al. The metal films are covered with  $\alpha$ - $\text{Al}_2\text{O}_3$ . The (0001) facet is in contact with the metal and is exposed to vacuum, except for the case with  $\Sigma_3$  (001)

grain boundaries which run parallel to the (0001) plane (Fig. 2b).<sup>82</sup> The  $x$ -dimension of this grain boundary simulation cell is kept at the bulk crystal values while the  $y$ -dimension, perpendicular to the grain boundaries, is obtained by optimizing a simulation cell with only the oxide present. This mimics isolated grain boundaries, which should not affect the lattice dimension parallel to it in a crystal of infinite size.

Next we discuss the details of the metal/oxide interfacial structures, which have not been elucidated in experiments for all metal and/or oxide facets. Even the widely adopted “Al-termination” configuration for the most-studied interface ( $\alpha$ -Al<sub>2</sub>O<sub>3</sub>(0001)/Al(111)) has been constructed with a fixed stoichiometry and does not allow the number of Al atoms in the surface unit cell to vary, e.g., at constant Al chemical potential via a Grand Canonical Ensemble simulation, which would be the most rigorous approach. Our Al(111)/ $\alpha$ -Al<sub>2</sub>O<sub>3</sub> structure (Fig. 2a) is based on the “FCC” interface structure<sup>29</sup> but adopts a doubled surface unit cell of lateral dimension  $4.81 \times 8.33 \text{ \AA}^2$ .<sup>24</sup> For this cell, we conduct a 1.7 ps *ab initio* molecular dynamics (AIMD) at T=400 K followed by quenching to T=0 K to equilibrate the Al(111)| $\alpha$ -Al<sub>2</sub>O<sub>3</sub>(001) interface before optimizing the atomic configuration.<sup>46</sup> In the appendix, we use a combinatorial approach to compare the structure with other interfacial models investigated in the literature.<sup>24–31</sup> As Ref. 24 points out, variations in the interfacial structure can change the work function by  $<0.5 \text{ eV}$ .

A similar AIMD procedure is applied to construct the Au(111)| $\alpha$ -Al<sub>2</sub>O<sub>3</sub>(001) interface (Fig. 2c); this model is meant to mimic Al<sub>2</sub>O<sub>3</sub> grown on AlAu<sub>4</sub> intermetallic surfaces.<sup>83,84</sup> The interface model with grain boundaries (Fig. 2b) is too large and costly to permit AIMD pre-equilibration. For this model we displace the oxide and metal in the lateral directions and show that the displacements only weakly affect the work function in the appendix.  $\gamma$ -Al<sub>2</sub>O<sub>3</sub> surfaces have been the subjects of DFT studies, but more than one atomic interpretations of the structure have been reported.<sup>33,70,71,85</sup>  $\gamma$ -Al<sub>2</sub>O<sub>3</sub> may be a better model for amorphous oxide, and will be considered in future work.

The number of water molecules residing on the outer surface of the oxide film depends on the humidity. Most existing computational work on explicit Al|Al<sub>2</sub>O<sub>3</sub> interfaces<sup>24,30,65</sup> have omitted H<sub>2</sub>O molecules. We include a submonolayer of H<sub>2</sub>O not only because of the finite humidity, but also because on some Al<sub>2</sub>O<sub>3</sub> surface facets, the oxides can exhibit metallic behavior at their outer (vacuum) surfaces in the absence of H<sub>2</sub>O or other solvent molecules when the inner oxide surfaces are in contact with electronegative metal.<sup>46</sup> As an

approximation of the finite temperature water film, we consider  $T=0$  K conditions, add sufficient  $\text{H}_2\text{O}$  molecules so each surface Al cation is coordinated to the O-atom of 1-3 water molecules, and optimize the atomic configurations. Some  $\text{H}_2\text{O}$  molecules spontaneously react with the surface and dissociate into two AlOH groups. In Fig. 2a, each exposed  $\text{Al}^{3+}$  on the surface is coordinated to 3  $\text{H}_2\text{O}$  molecules, one of which is spontaneously hydrolysed, i.e., it transfers a proton to a surface  $\text{O}^{2-}$  otherwise bonded to 3  $\text{Al}^{3+}$ . In Fig. 2c, each exposed 3-coordinated  $\text{Al}^{3+}$  is coordinated to an  $\text{H}_2\text{O}$  molecule, which is hydrogen-bonded to another adsorbed, hydrolysed  $\text{H}_2\text{O}$  (i.e., OH group). 50% of the  $\text{H}_2\text{O}$  are hydrolysed. In Fig. 2b, each exposed  $\text{Al}^{3+}$  on the surface is coordinated to one OH from an  $\text{H}_2\text{O}$  which has donated an  $\text{H}^+$  to a surface  $\text{O}^{2-}$ ; this newly created OH group is coordinated to another  $\text{H}_2\text{O}$  molecule via hydrogen bonding. 37.5 % of the adsorbed  $\text{H}_2\text{O}$  molecules are hydrolysed. Like at the metal/oxide interface, we do not claim to have found the most stable  $\text{H}_2\text{O}$  adsorption configuration on all  $\text{Al}_2\text{O}_3$  surface facets; some of our  $\text{H}_2\text{O}$  configurations may be metastable. Instead, we vary the interfacial structures and examine the differences in the appendix, where we show that a change in the  $\text{H}_2\text{O}$  structure can give rise to a  $>1$  eV change in the work function and a similar global shift in the band structure,<sup>86</sup> but this does not strongly affect the metal/oxide band alignment. The different water terminations in Fig. 2a and Fig. 2c help illustrate this point.

In some cases, surface proton vacancies are introduced by removing H atoms from  $\text{H}_2\text{O}$  on the oxide outer surface; these H are chosen at spatially separated locations (Fig. 3). In Fig. 3a-d,  $\text{H}^+$  are removed from  $\text{H}_2\text{O}$  molecules; these OH groups newly created are coordinated to a single  $\text{Al}^{3+}$ . In Fig. 3e-f,  $\text{H}^+$  are removed from  $\text{O}^{2-}$ , coordinated to three  $\text{Al}^{3+}$  cations, which are part of the  $\text{Al}_2\text{O}_3$  surface prior to addition of water; hence no new OH group is created. These deprotonation schemes are solely meant to mimic the electrostatic environments arising from negatively-charge salt anions not present in our simulations; the precise locations of deprotonated sites will have quantitative effects but qualitatively speaking they are not considered critical.

$V_{\text{O}}$  is introduced by removing one oxygen atom each at various positions in the crystalline oxide film. We assume that the atomic length-scale structural heterogeneity at the metal/oxide interface does not strongly affect  $V_{\text{O}}$  properties, and that each O-atom removed is representative of all  $V_{\text{O}}$  at that  $z$  position. This is one advantage of crystalline oxide models; in amorphous  $\text{Al}_2\text{O}_3$  films,  $V_{\text{O}}$  formation energies may not systematically vary with  $z$ .



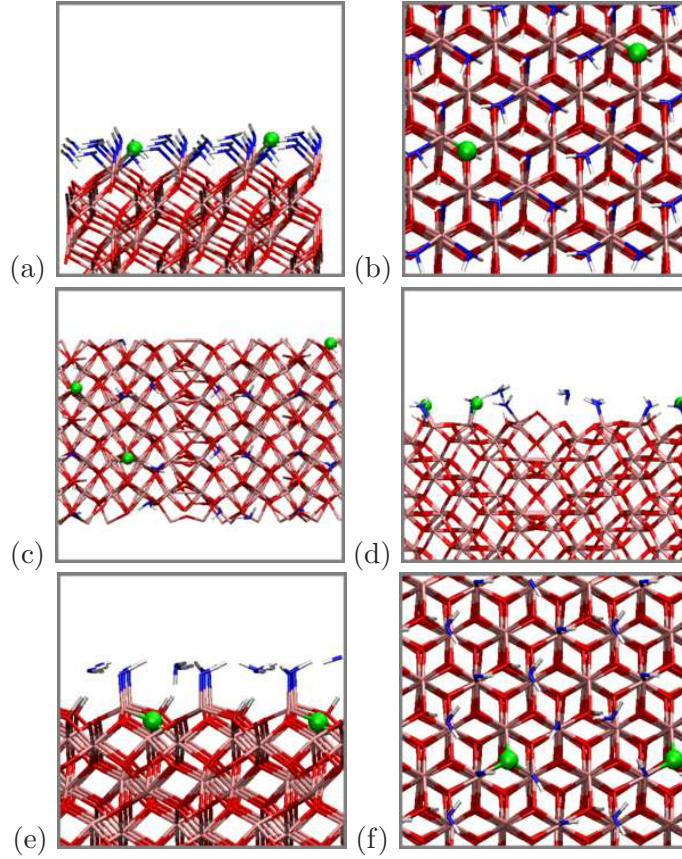
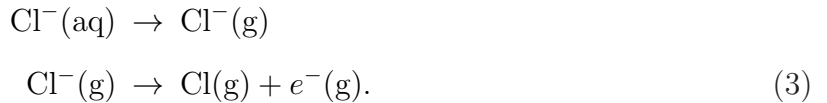


FIG. 3: Detailed atomic structures at deprotonated surfaces. (a)-(b)  $\alpha$ - $\text{Al}_2\text{O}_3$  (001) on Al(111) and correspond to Fig. 2a; (c)-(d)  $\alpha$ - $\text{Al}_2\text{O}_3$  with grain boundary on Al(111) (Fig. 2b); (e)-(f)  $\alpha$ - $\text{Al}_2\text{O}_3$  (001) on Au(111) (Fig. 2c). Pink, red, and blue depict Al, O, and O(water) atoms. Green spheres depict O atoms from which  $\text{H}^+$  are removed.

The exception is Fig. 2b, where  $V_{\text{O}}$ 's along the grain boundary are different from  $V_{\text{O}}$  in bulk-like oxide regions; only the former are considered.

$\text{Cl}^-$  are inserted into these  $V_{\text{O}}^{q+}$ ; in effect, they substitute for O in the lattice. Calculating  $\text{Cl}^-$  insertion energetics involves the following steps in a thermodynamic cycle:



Here “(g)” denotes the gas phase. The two steps in Eq. 3 yield the  $\text{Cl}^-$  dehydration free energy ( $\Delta G_{\text{hyd}} = -3.32$  eV),<sup>87</sup> and the electron affinity (EA) of the Cl atom in vacuum, respectively. Using the PBE functional and a  $10 \text{ \AA}^3$  simulation cell with one  $\text{Cl}^-$ , we predict that EA for  $\text{Cl}^-$  is 3.42 eV. It is 0.20 eV below the experimental gas phase value of 3.62-3.72 eV;<sup>88</sup>

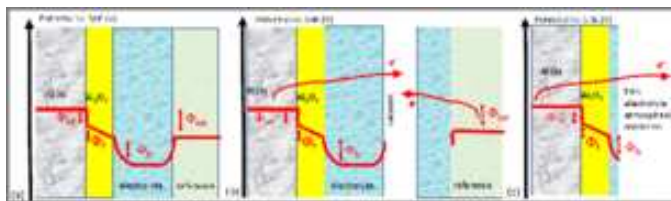


FIG. 4: (a)-(c) Definitions of the  $\Phi_{mf}$ ,  $\Phi_f$ , and  $\Phi_{fs}$  contributions to the total potential in full and half cell configurations.

here we adopt a 3.62 eV value.

To examine  $\text{Cl}^-$  replacing surface  $\text{OH}^-$  groups (Eq. 2), we apply  $\alpha\text{-Al}_2\text{O}_3$  (0001) slabs with no metal present; this is adequate because no  $e^-$  is transferred alongside these substitutions (Eq. 2). The standard state (1.0 M concentration)  $\text{OH}^-$  hydration free energy, needed here, is -4.53 eV taken from the literature.<sup>89</sup> Other simulation cells contain only  $\alpha\text{-Al}_2\text{O}_3$  in bulk crystal configurations. These are used to compare the band structures and charge-neutral oxygen vacancy orbital energy levels of the oxide computed using the PBE and the more accurate HSE06 functionals via Fig. 1a-c.

We apply the Bader charge method<sup>90</sup> to examine the change of charge distribution in the different zones of the slab models arising from insertion of  $\text{Cl}^-$  into  $\text{V}_\text{O}^{2+}$  or deprotonation on the hydroxylated oxide surface. The three relevant zones “Z” are metal, oxide, and surface water (which may be hydrolysed, split into  $\text{H}^+$  and  $\text{OH}^-$ ). Bader charges, like all charge-decomposition schemes, are approximate, especially given the fact that Al metal ions at the interface may be assigned partial charges. To facilitate analysis, we only consider changes in charge in a zone ( $\Delta c(Z)$ ) relative to a reference. For each system with surface deprotonation but no  $\text{Cl}^-$ , the reference is the same slab but without surface deprotonation. For each system with  $\text{Cl}^-$  inserted into a  $\text{V}_\text{O}$ , the reference is the slab with the same amount of surface deprotonation but no  $\text{Cl}^-$  or  $\text{V}_\text{O}$ . We also assign all metal atoms to be in the metal zone, including  $\text{Al}^{3+}$  inside the oxide. This is reasonable because Al only exists as  $\text{Al}^{3+}$  inside the oxide and are found to exhibit zero Bader charges. At the metal/oxide interface, it is difficult to definitively assign whether a Al atom is in the metal or the oxide zone; our scheme circumvents this ambiguity.

## B. Band Alignment and Voltage

In this section, we emphasize that local contributions to the voltage are more relevant to  $V_O$  charging than the applied voltage ( $\Phi_{\text{ext}}$ ) itself.

Experimentally, voltage differences are measured using a reference electrode, which exhibits a  $E_F$  different from the working electrode. The applied voltage  $\Phi_{\text{ext}}$  contains several contributions (Fig. 4a):

$$\Phi_{\text{ext}} = \Phi_{\text{mf}} + \Phi_{\text{f}} + \Phi_{\text{fs}}, \quad (4)$$

Here “m” denotes metal, “f” is the oxide film, “s” is the “solution” or electrolyte, and “mf” and “fs” are the interfaces. Fig. 4b closely resembles the voltage construction in the point defect model (Fig. 2 in Ref. 3). These voltage contributions are also discussed in Ref. 37, which however does not apply DFT calculations with explicit electric fields across the oxide layer.

DFT is an electronic structure ground state theory and supports only one  $E_F$ . The most readily available reference “electrode” is vacuum. We inject vacuum into the liquid electrolyte region (Fig. 4b); this step is formally exact. Then, in Fig. 4c, the reference electrode is replaced by vacuum, and the absolute voltage referenced against SHE ( $\mathcal{V}_e$ ) replaces  $\Phi_{\text{ext}}$  in Fig. 4a-b. Following the Trasatti convention,<sup>91</sup> we define

$$\mathcal{V}_e = W/|e| - 4.44 \text{ V}, \quad (5)$$

where  $|e|$  is the electronic charge,  $W = -E_F$  is the work function, and  $E_F$  is referenced to vacuum. The work function is cumulatively modified by the electric double layer (EDL) at each interface.

An important question is whether the model system – which does not include a liquid electrolyte – gives a structure/voltage relation that mimics experimental conditions. Our simplified electrolyte models consist of sub-monolayer  $\text{H}_2\text{O}$  on the oxide surface optimized at  $T=0$  K. In the appendix, it is shown that this approach is unlikely to provide useful comparison with the electrochemical measured  $\mathcal{V}_e$  or  $\Phi_{\text{ext}}$ , or for that matter Kelvin Probe Force Microscopy (KPFM) measurements of work functions in vacuum environments.<sup>92</sup> The reason is that, on  $\text{Al}_2\text{O}_3$  surfaces, the oxide-solvent term  $\Phi_{\text{fs}}$  is very sensitive to the surface water coverage, structure, and presence/absence of hydrolysis events ( $\text{H}_2\text{O} + >\text{AlO} \rightarrow 2 >\text{AlOH}$ ). Instead, we will assume a voltage of -0.50 V vs. SHE to mimic the onset of pitting,<sup>19</sup>

and ignore the computed  $\mathcal{V}_e$  (Eq. 5) for the purpose of evaluating Eq. 1. Despite this, the calculated  $\mathcal{V}_e$  will prove to be a useful measure of convergence with respect to simulation cell size. Calculating accurate  $\mathcal{V}_e$ 's for oxide-covered metal surfaces remains a challenge that will require more future work (Sec. IV).

The more relevant point about voltage dependence is that  $\mathcal{V}_e$  or  $\Phi_{\text{ext}}$  is made up of several interfacial components (Eq. 4), none of which has been separately measured. The appendix will show that the contact potential at the Al/Al<sub>2</sub>O<sub>3</sub> metal-film interface ( $\Phi_{\text{mf}}$ ) and the voltage drop in the oxide film ( $\Phi_{\text{f}}$ ) most strongly affect the energy levels of orbitals associated with the valence band edge relative to the V<sub>O</sub> energy level ( $E_{\text{V}_0\text{VBE}}$ ) or relative to  $E_{\text{F}}$  ( $E_{\text{FVBE}}$ ). In contrast, the potential drop at the oxide/solvent interface ( $\Phi_{\text{fs}}$ ), which resides on the side of the oxide film opposite to the metallic region (Fig. 4c), does not significantly affect  $E_{\text{V}_0\text{VBE}}$  or  $E_{\text{FVBE}}$ , as long as the oxide/vacuum interface has no net charge. The fact that a charge-neutral liquid electrolyte, not included in our models, supplies only a global shift of the band structure is taken as justification of our replacement of the predicted  $\mathcal{V}_e$  with  $\mathcal{V}_e = -0.5$  V vs. SHE.

A charge-neutral metal surface and a charge-neutral oxide film yields  $\Phi_{\text{f}} = 0$  V. As will be shown, this is not sufficient to generate charged V<sub>O</sub>. Finite  $\Phi_{\text{f}}$  is created by deprotonating one or more H<sub>2</sub>O at the film/solvent interface, creating a net negative surface charge density. Because the DFT simulation cell is charge-neutral, this should induce positive charges at the metal/film interface. The H<sup>+</sup> vacancies change the average dipole surface density  $d$  in the direction perpendicular to the interface. A positive change in  $d$  increases the voltage according to the equation<sup>46</sup>

$$\Delta\mathcal{V}_e = 4\pi\Delta d/A, \tag{6}$$

where  $A$  is the lateral surface area. Eq. 5 can be readily evaluated in simulation cells with a vacuum region. Compared to other DFT formulations in the literature, we control  $\mathcal{V}_e$  using  $e^-$  and atoms,<sup>34,93-97</sup> not effective medium approaches extrinsic to standard DFT.<sup>98-101</sup>

### C. System Size Effects

A V<sub>O</sub><sup>2+</sup> residing in the electronically insulating oxide film should also induce a negative surface charge on the metal slab in contact with it in the charge-neutral simulation cell. The charge separation leads to a significant dipole moment along the  $z$ -direction. We apply

the standard dipole correction to remove the electrostatic coupling between periodic images in the  $z$  direction, separated by the vacuum region.<sup>102</sup> However, the cell is also periodically replicated in the lateral dimensions. The lateral images of the dipole moment repel one another.<sup>103</sup> These spurious electrostatic couplings decrease with the lateral cell area  $A$ . Hence we systematically increase the lateral cell dimensions with area  $A$  while keeping a single  $V_O^{2+}$  or  $Cl^-$  in the cell.

Another manifestation of system size effect is that  $\mathcal{V}_e$  may depend on  $A$ . Benchtop corrosion experiments are often performed at constant voltage conditions. In DFT calculations, introducing a single charged  $Cl^-$  or  $V_O^{2+}$  should occur at constant  $\mathcal{V}_e$  in the limit of infinite  $A$  (Eq. 6). At finite  $A$ , however,  $\mathcal{V}_e$  is modified by the introduction of charged defects. Systematically increasing  $A$  lessens this problem. The quantum continuum approach<sup>45</sup> or local charge compensation methods<sup>104</sup> may also be applied to maintain the system at the same  $\mathcal{V}_e$  without system size increase. These methods, which require extensions to standard DFT codes, will be considered in the future.

In contrast, a charge-neutral defect like  $V_O$  is not associated with a net charge transfer or change in dipole moment  $d$ . The resulting band structure should be insensitive to  $A$ .

### III. RESULTS

#### A. Oxygen Vacancies without Interfaces; Interfaces without Vacancies

Our goal is to study simulation cells with both explicit interfaces and defects. But in this section, we first examine the orbital energy level of a charge-neutral  $V_O$  in crystalline  $\alpha\text{-Al}_2\text{O}_3$  relative to the valence band edge (VBE) ( $\Delta E_{V_O\text{VBE}}$ ) without Al metal present (Fig. 1c), as well as the band offset and the contact potential between  $\text{Al}(111)$  and  $\alpha\text{-Al}_2\text{O}_3(111)$  in the absence of  $V_O$  (Fig. 1b). This two-step scheme uses smaller simulation cells, so that comparison of PBE calculations with those using the more computationally costly HSE06 DFT functional can be made. PBE underestimates band gaps and defect orbital energy levels inside the gap. HSE06 generally predicts more accurate orbital alignment, but it is challenging to apply to systems with 800+ atoms like the interfacial cells which can accommodate  $V_O$  (Table I). Subtracting  $\Delta E_{V_O\text{VBE}}$  from the offset between the Fermi level and the VBE ( $\Delta E_{F\text{VBE}}$ ), computed in two different simulation cells, gives an approximate

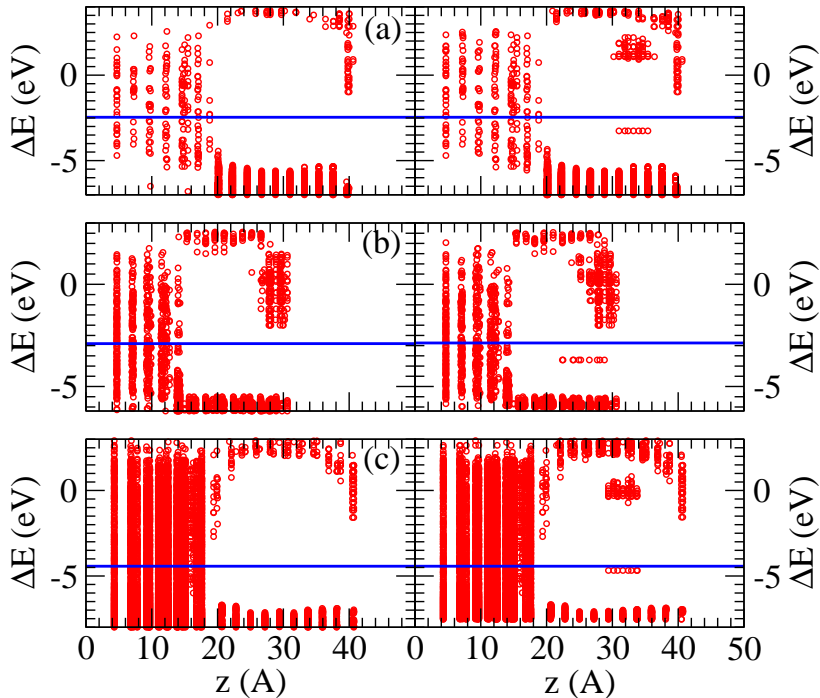


FIG. 5: LDOS of interfacial systems considered in this work. (a)  $\alpha$ - $\text{Al}_2\text{O}_3$  (001) on Al(111); (b)  $\alpha$ - $\text{Al}_2\text{O}_3$  with grain boundary on Al(111); (c)  $\alpha$ - $\text{Al}_2\text{O}_3$  (001) on Au(111). The left and right panels are with and without  $V_{\text{O}}$ , respectively. No  $\text{H}^+$  vacancy exists on any surface in this figure. Red circles represent atoms on which a Kohn-Sham orbital at a certain energy exceed  $>0.2\%$ . In vacuum regions, no atoms exist and no LDOS is represented therein.

alignment between  $V_{\text{O}}$  orbitals and the Fermi level. However, this two-step approximation is not valid when charge transfer occurs (e.g., if a  $V_{\text{O}}^{2+}$  is present), and/or when an electric field exists across the oxide film.

Details of the  $\alpha$ - $\text{Al}_2\text{O}_3$  cell with one charge neutral  $V_{\text{O}}$  is described in Table I. The  $V_{\text{O}}$  is occupied by two  $e^-$  and is an “ $f$ -center.” The  $2 \times 2 \times 2$  Brillouin zone sampling yields 6 special  $k$ -points. Near the band gap, the energy level of each orbital differs by at most 0.04 eV at different  $k$ -points. Hence it is a good approximation to report these values averaged over the 6  $k$ -points, instead of computing the entire band structure of this supercell and searching for the absolute VBE. We find that  $\Delta E_{V_{\text{O}}V_{\text{BE}}} = 2.34$  eV and 3.12 eV for PBE and HSE06, respectively. These values are in good agreement with the literature.<sup>38–42</sup> Increasing the cell

size from  $\text{Al}_{48}\text{O}_{72}$  to  $\text{Al}_{108}\text{O}_{162}$  yields similar PBE results.

Regarding  $\Delta E_{\text{FVBE}}$  at explicit  $\text{Al}(111)/\alpha\text{-Al}_2\text{O}_3(0001)$  interfaces, the PBE and HSE06 values are 2.94 eV and 4.08 eV, respectively. As expected, HSE06 increases the band gap and shifts the valence band to lower energy levels compared to PBE. Combining these results and  $\Delta E_{\text{V}_0\text{VBE}}$ , the two functionals predict that  $\text{V}_0$  sits 0.60 eV and 0.96 eV below  $E_{\text{F}}$ , respectively (Fig. 1d-f). Switching to HSE06 thus lowers the occupied  $\text{V}_0$  orbital level by -0.36 eV relative to the Fermi level. It would take an extra +0.36 V applied potential to shift this orbital level, computed using PBE, to a regime where it will begin to be oxidized (i.e., lose  $e^-$  and acquire positive charge(s)) if we were to use the more accurate HSE06 functional. Since one of our main theses is that it is more difficult to create positively-charged  $\text{V}_0$  than is assumed in the literature, switching to the more accurate HSE06 functional will only reinforce this conclusion. In the remainder of this paper, we will apply the PBE functional, for which  $\Delta E_{\text{V}_0\text{VBE}} < 2.34$  eV is a zeroth-order guide for the orbital level of uncharged  $\text{V}_0$ .

$\Delta E_{\text{FVBE}}$  contains a contribution from the metal/oxide contact potential ( $\Phi_{mf}$ , Fig. 4a-c).<sup>37</sup>  $\Phi_{mf}$  can be computed by subtracting the work function in presence of an oxide film from the work function in the absence of oxide coating the metal surface, as long as the oxide slab does not exhibit a net dipole moment. PBE and HSE06 yield -0.50 V and -0.68 V, respectively. The HSE06 value is larger by 36%; this ratio is larger than that between HSE06 and PBE values at the Li metal/LiF (001) interface.<sup>46</sup>

### B. Oxygen Vacancies are Charge Neutral when $\Phi_{\text{f}}=0$ (no surface deprotonation)

Next we consider other metal/oxide interfaces in larger simulation cells. The panels on the left hand side of Fig. 5 depict the local electronic densities of state (LDOS) in interfacial supercells without a  $\text{V}_0$ . The valence band edges are flat across the oxide film region, corresponding to a no-electric field ( $\Phi_{\text{f}}=0$ , Fig. 4c), “flat band” condition.<sup>45</sup>  $\Delta E_{\text{FVBE}}$  are 2.94 eV, 1.52 eV, and 2.49 eV, respectively, in Fig. 5a-c. The  $\alpha\text{-Al}_2\text{O}_3$  cases (a) and (c) are higher than  $\Delta E_{\text{V}_0\text{VBE}}$  2.34 eV, and are consistent with  $\text{V}_0$  residing below the Fermi level in DFT/PBE calculations. We have not calculated  $\Delta E_{\text{V}_0\text{VBE}}$  for (b) because, unlike in oxide films with no defects, this quantity should depend on the spatial position of the  $\text{V}_0$  and is not single-valued.

The right hand side panels represent configurations with an explicit  $\text{V}_0$  each in the oxide

film. Their locations are illustrated in Fig. 6. In all cases, the orbitals associated with the  $V_O$  lie below  $E_F$ . This is consistent with the  $E_{V_O VBE}$  plus  $E_{F_0 VBE}$  estimate applied to the left hand side panels without  $V_O$  in the cells. The  $V_O$  orbital level associated with Au(111) (Fig. 5c) is closer to  $E_F$  than on Al(111) (Fig. 5a), consistent with the fact that Au is more electropositive and exhibits less tendency to emit electrons. These findings constitute the main result of this paper.

The above conclusion that  $V_O$  lies below  $E_F$  does not qualitatively depend on the spatial location of the  $V_O$ . In the case of Fig. 5b, moving the  $V_O$  within the grain boundary from  $z=26.5 \text{ \AA}$  to  $22.4 \text{ \AA}$ ,  $18.3 \text{ \AA}$ , or  $16.4 \text{ \AA}$  ( $\Delta z=12.4, 8.3, 4.2, \text{ or } 2.3 \text{ \AA}$ , Fig. 5) changes the offset between  $E_F$  and the  $V_O$  orbital level from  $-0.80 \text{ eV}$  to  $-0.27 \text{ eV}$ ,  $-0.44 \text{ eV}$ , and  $-0.55 \text{ eV}$ . Here  $\Delta z$  is the vertical distance of the  $V_O$  from the metal/oxide interface, which is defined as the  $z$ -position of the lowest lying plane containing oxygen atoms. The total energies of these systems are increased relative to that of the  $V_O$  at the outermost  $z=26.5 \text{ \AA}$  position by  $0.31 \text{ eV}$ ,  $0.30$ , or  $0.22 \text{ eV}$  respectively; the small energy changes are likely due to non-constant strain effects at different film depths. For the  $V_O$  at  $z=22.4 \text{ \AA}$  ( $\Delta z=12.4 \text{ \AA}$ ), we also apply spin-polarized DFT to explore the possibility of a spin-polarized  $V_O^+$  vacancy. No charged  $V_O$  is observed. This spin-polarization issue may be reconsidered in the future using hybrid DFT.

As discussed in Sec. II A, the atomic length-scale structure at the metal/oxide interface is not known from experiments. This may give rise to uncertainties in DFT-predicted  $\Phi_{mf}$  on the order of  $<0.5 \text{ V}$ .<sup>24,30</sup> However, even a  $+0.5 \text{ V}$  shift in  $\Phi_{mf}$  does not change the qualitative DFT/PBE conclusion about  $V_O$  if we include the  $0.36 \text{ eV}$  HSE06 correction (Sec. III A). We find that increasing the lateral system size by doubling the  $x$ - or  $y$ -dimension by a factor of two yields no qualitative and minimal quantitative changes in these conclusions about uncharged  $V_O$ , as anticipated in Sec. II C.<sup>50</sup>

Finally, we discuss  $\mathcal{V}_e$  predictions. The voltages  $\mathcal{V}_e$  associated with the left side of Fig. 5a-c are  $-1.98 \text{ V}$ ,  $-1.54 \text{ V}$ , and  $-0.01 \text{ V}$ , respectively. The corresponding  $\mathcal{V}_e$  on the right hand side of these panels, where  $V_O$  exist, are almost unchanged. However, the appendix shows that such  $\mathcal{V}_e$  are very sensitive to the  $H_2O$  adsorption configuration, especially when hydrolysis event occurs, leading to global shifts in the electronic band structure due to the change in  $\Phi_{fs}$  (Fig. 4). This is unlike the case of organic solvent electrolytes used in batteries.<sup>46</sup> One reason is that each water hydrolysis event causes significant charge separation. Hence these



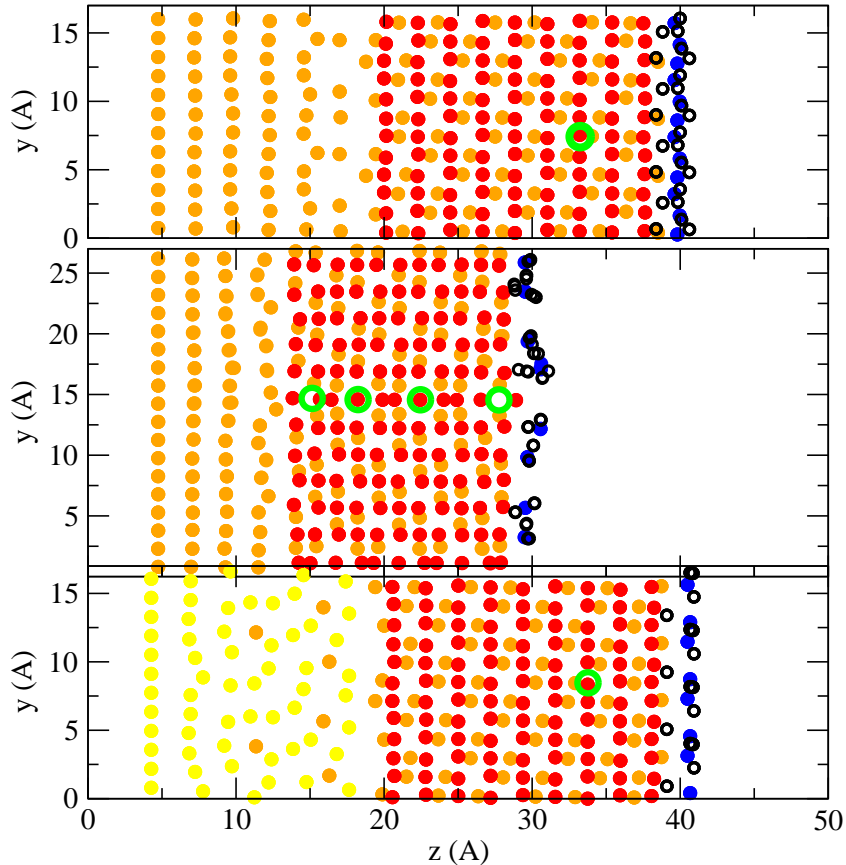


FIG. 6: Illustrations of the positions of the  $\text{Cl}^-$  and  $\text{V}_\text{O}$  discussed in the text. The three panels correspond to Fig. 2a-c, respectively. Orange, red, blue, yellow, hollow black, and hollow green circles refer to Al, O, O(water), Au, H, and Cl atoms, respectively.

$\mathcal{V}_e$  cannot be considered definitive, nor should they be compared with experiments.

### C. Charged Oxygen Vacancy Exists With Field in Oxide Film (with surface deprotonation)

Next we show that a positive electric field pointing from metal to outer oxide film surface can create doubly charged oxygen vacancies. Electric fields within the oxide can be caused by an enhanced concentration of cations or anions at the liquid-solid interface. Since ions and liquid electrolytes are excluded from our calculations, we instead create 2-3 H-vacancies

among AlOH groups on the outer surface, forming  $\text{AlO}^-$  (Sec. II A). These  $\text{AlO}^-$  groups should induce a compensating positive charge on the metal/oxide interface, a positive electric field, and an increased  $\mathcal{V}_e$  via Eq. 6. If a charged  $\text{V}_\text{O}^{2+}$  is present, it should provide a partial balancing charge for the  $\text{AlO}^-$  surface groups.

Fig. 7a-c correspond to Fig. 5a-c, except that the LDOS for an O-vacancy closer to the metal surface than the one in Fig. 5b is depicted in Fig. 7b (see below). The left hand column depicts LDOS with a field but without  $\text{V}_\text{O}$ . The valence band edges show that potential gradients indeed exist. Note that the field directions and the slopes associated with  $\Phi_f$  are opposite to those depicted in Fig. 1a-c or in classic PDM schematics.<sup>3,37</sup> The computed  $\mathcal{V}_e$  of these systems are 0.96 V, 0.62 V, and 2.54 V, respectively. They are much higher than those associated with Fig. 5; the changes are  $\Delta\mathcal{V}_e=+2.94$  V,  $+2.16$  V, and  $+2.55$  V. Experimentally, raising the voltage is consistent with increased pitting corrosion. As discussed in Sec. II B, we do not claim that our computed  $\mathcal{V}_e$  are quantitative.

Table II depicts the changes in aggregate Bader charges ( $\Delta c(Z)$ ) in the zones  $Z$ =metal, oxide, and water due to surface deprotonation in systems without oxygen vacancies. With the  $\alpha\text{-Al}_2\text{O}_3$  slabs on Al(111) and Au(111) metal surfaces (Fig. 2a, Fig. 2c), there are approximately  $+2|e|$  charges induced in the metal zone, where  $|e|$  is the electronic charge. This is reasonable because the two H-atoms removed on the surface are expected to be  $\text{H}^+$ , inducing equal but opposite charge in the metal zone. The demarcation of charges in the oxide and water zones appears more ambiguous, partly because of hydrolysis reactions arguably turn some  $\text{O}^{2-}$  on the oxide surface into OH, but we have not reassigned atoms across zones. The grain boundary system (Fig. 2b) has three surface OH groups deprotonated, while the Bader analysis suggests that a  $+4|e|$  is induced on the metal zone. The ambiguity likely arises from assigning all metal atoms at the metal/oxide interface to the metal zone.

The right hand columns of Fig. 7 depict LDOS with an explicit  $\text{V}_\text{O}$  in each simulation cell. In all cases, the electric field has moved the orbitals associated with the defect into the gap, creating a  $\text{V}_\text{O}^{2+}$ . We also perform spin-polarized DFT calculations in Fig. 7b to check if singly charged  $\text{V}_\text{O}^+$  occurs. The result is the same as in the non-spin-polarized DFT calculation. Because of the potential gradient,  $\text{V}_\text{O}^{2+}$  more readily occurs in the outer regions of the oxide film. Moving the  $\text{V}_\text{O}$  to  $z=26.7$  Å ( $\Delta z=12.6$  Å) from where it is ( $z=18.2$  Å,  $\Delta z=4.1$  Å in Fig. 7b) raises the  $\text{V}_\text{O}$  vacancy to 1.98 eV above  $E_\text{F}$  instead of 1.24 eV above  $E_\text{F}$ . The orbital level associated with the  $\text{V}_\text{O}$  at  $z=26.7$  Å for the system with Au(111)

figure	deprot.	metal	oxide	water
Fig. 2a	2	+1.52	-0.28	-1.26
Fig. 2b	3	+3.95	-1.43	-2.52
Fig. 2c	2	+1.65	0.56	-2.74

TABLE II: Change in charge in deprotonated slabs in each zone ( $\Delta c(Z)$  in units of  $|e|$ ), counting both electrons and nuclei, relative to the slab without deprotonation. No  $V_O$  or  $Cl^-$  exists in these slabs. The number of H atoms removed from the surface is “deprot.”

almost merges with the conduction band, and is not shown; instead Fig. 7c depicts the LDOS of a  $V_O$  closer to the metal surface, at  $z=18.2 \text{ \AA}$ .

As mentioned in Sec. II C, simulation size effects is more important when charged defects exist. Doubling one of the lateral dimensions of the simulation cell associated with Fig. 7b is found to yield a charged  $V_O$  orbital level at 1.27 eV above  $E_F$ . This  $\Delta E_{FVBE}$  is only 0.05 eV higher than that for the smaller cell size. However, for Fig. 7c, doubling the system size increases  $\Delta E_{FVBE}$  from 1.00 eV to 1.85 eV. These variations are not straight-forward to analyze because there are charges on the oxide outer surface, in the  $V_O^{2+}$ , and at the metal-film interface. Regarding Fig. 7b, moving the  $V_O^{2+}$  from  $z=26.7 \text{ \AA}$  ( $\Delta z=12.6 \text{ \AA}$ ) to  $z=18.2 \text{ \AA}$  ( $\Delta z=4.1 \text{ \AA}$ ) leads to -4.18 eV and -4.59 eV changes in the total energy depending on whether we use the base simulation cell (Table I) or a cell doubled in the lateral dimension. In all these cases, increasing the cell size does not lead to the  $V_O^{2+}$  becoming charge neutral. Thus system size has quantitative but no qualitative effects. We have not considered  $Al^{3+}$  cation motion. However, such cations should also be attracted towards the negatively charged oxide surface and promote anodic corrosion when a high voltage is applied.

We conclude that  $V_O^{2+}$  most likely requires a positive electric field and a higher effective voltage than that under flat band conditions to exist. This view about  $Al_2O_3$  films on Al metal surfaces is predicated on the assumption that  $e^-$  can tunnel through the oxide and attain the electronic ground state. If the oxide is sufficiently thick, non-equilibrium electronic configurations may persist.

#### D. $Cl^-$ Electrochemical insertion into Oxygen Vacancies

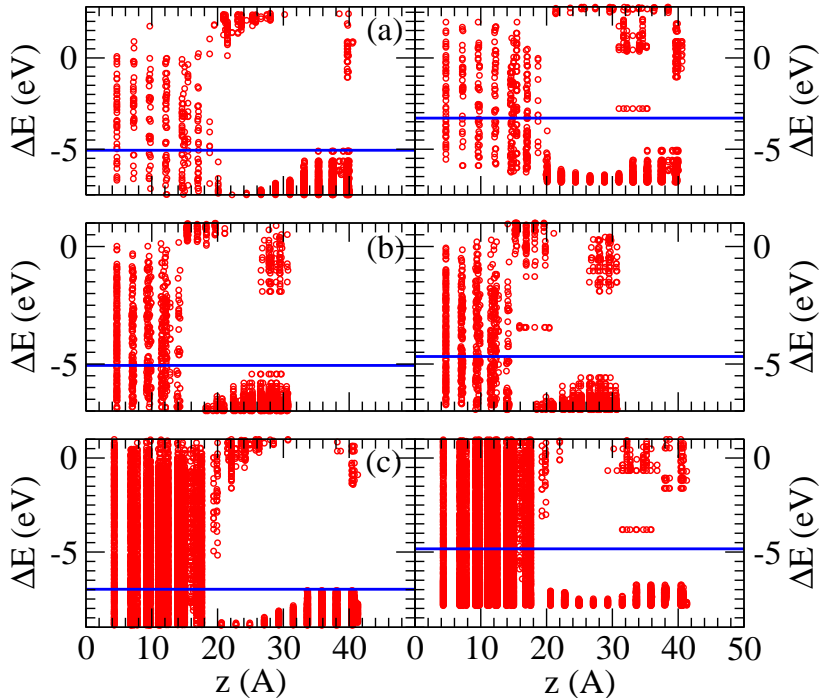
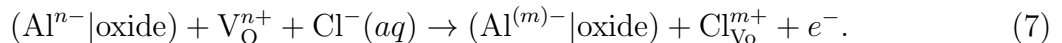


FIG. 7: LDOS of interfacial systems considered in this work. (a)  $\alpha$ - $\text{Al}_2\text{O}_3$  (001) on Al(111); (b)  $\alpha$ - $\text{Al}_2\text{O}_3$  with grain boundary on Al(111); (c)  $\alpha$ - $\text{Al}_2\text{O}_3$  (001) on Au(111). Red circles denote atoms with Kohm-Sham orbital contributions exceeding 0.2%. The right hand column panels contain a  $V_{\text{O}}$  while the left hand columns do not. Unlike Fig. 5, there are 2-3  $\text{H}^+$  vacancies on the outer surfaces of the oxides.

Next we consider the energetics of  $\text{Cl}^-$  insertion into pre-existing  $V_{\text{O}}$ , charged or otherwise (Eq. 1). Unlike Sec. III B and III C, simulation cells both with and without surface charges are considered. We assume that oxygen vacancies in the oxide film are not mobile within the time scale of Cl insertion.  $\text{Cl}^-$  insertion kinetics are not considered in this work. The overall change in the charge-neutral simulation cell is



The  $e^-$  released on the right side goes to  $E_{\text{F}}$  in the Al metal region, effectively “outside” the simulation cell, yielding an energy gain that is equal to  $|e|E_{\text{F}}$ . As discussed in Sec. II B, we impose  $\mathcal{V}_e = -0.50$  V vs. SHE, which corresponds to  $E_{\text{F}} = -3.94$  eV, instead of using the  $\mathcal{V}_e$

and  $E_F$  computed for each slab.

First we consider no surface deprotonation, in which case the  $V_O$  are uncharged hosts. With the  $E_F$  and  $\Delta G_{\text{hyd}}$  discussed above, and other input listed in Sec. II A, the energies of inserting a  $\text{Cl}^-$  into the  $V_O$  associated with Fig. 5a-c are  $\Delta E_{\text{Cl-O}} = +1.14$  eV,  $+0.54$  eV, and  $+0.61$  eV at  $-0.50$  V vs. SHE. Applying a voltage  $> -0.5$  V (higher work function) would further favor Eq. 7.  $\text{Cl}^-$  is a larger anion than oxygen, and inserting  $\text{Cl}^-$  into  $V_O$  in the dense  $\alpha\text{-Al}_2\text{O}_3$  proves less energetically favorable than into  $V_O$  in the grain boundary (Fig. 5b), where there is more space. Focusing on the grain boundary in  $\alpha\text{-Al}_2\text{O}_3$ , inserting  $\text{Cl}^-$  into  $V_O$  at distances progressively closer to the oxide outer surface  $z = 15.7$  Å,  $18.2$  Å,  $22.4$  Å, and  $26.5$  Å ( $\Delta z = 1.6$  Å,  $4.1$  Å,  $8.3$  Å, and  $12.4$  Å respectively) yields  $\Delta E_{\text{Cl-O}} = -0.21$  eV,  $-0.24$  eV,  $-0.22$  eV, and  $+0.54$  eV. These energies are similar except when  $\text{Cl}^-$  is near the oxide surface.

These  $\Delta E_{\text{Cl-O}}$  values are computed using the baseline simulation cells (Table I). Table III shows that both  $\Delta E_{\text{Cl-O}}$  and the calculated voltage  $\mathcal{V}_e$  can exhibit some dependence on the lateral surface area of the simulation cell, as anticipated in Sec. II C. The convergence rates are not uniform and depend on materials and location of the  $\text{Cl}^-$ . However, in the  $2 \times 2$  supercells where the lateral cell sizes exceed  $30$  Å,  $\Delta E_{\text{Cl-O}}$  converge to within  $0.06$  eV, while  $\Delta \mathcal{V}_e$ , which measure the difference in  $\mathcal{V}_e$  with and without the  $\text{Cl}^-$ , trend towards zero as they should. This suggests that the largest simulation cells considered in Table III, containing 3000-4000 atoms, are sufficient for computing  $\text{Cl}^-$  insertion energies in most cases. More significantly,  $\text{Cl}^-$  insertion into the grain boundary (Fig. 5b) is found to be energetically favorable at an applied  $-0.50$  V voltage, as long as it is sufficiently far from the surface. Special care is taken to ensure that, as the simulation cells are expanded in the lateral directions, the water configurations are unchanged.

Next we consider  $\text{Cl}^-$  insertion into  $V_O^{2+}$  in two selected cases. Adding a  $\text{Cl}^-$  to the  $V_O^{2+}$  at  $z = 18.2$  Å ( $\Delta z = 4.1$  Å) associated with Fig. 7b yields a  $-1.94$  eV exothermicity, compared with  $-0.24$  eV without deprotonation at the same lateral cell size. These results are in qualitative agreement with the perspective that higher applied voltages lead to more ready  $\text{Cl}^-$  insertion into passivating oxide films.<sup>14</sup> However, if the  $\text{Cl}^-$  were inserted into a  $V_O^{2+}$  at  $z = 26.5$  Å ( $\Delta z = 12.4$  Å),  $\Delta E_{\text{Cl-O}}$  is increased from  $-0.22$  eV without deprotonation to  $+0.84$  eV with protonation. This increase in  $\Delta E$  is likely the result of strong Coulomb repulsion between the  $\text{Cl}^-$  and the  $\text{AlO}^-$  groups at the surface. Since larger simulation

system	property	1×1	1×2	2×2
Fig. 2a	$\Delta E_{\text{Cl-O}}$	+1.14 eV	+0.93 eV	+0.89 eV
	$\Delta \mathcal{V}_e$	-0.88 V	-0.50 V	-0.23 V
Fig. 2b	$\Delta E_{\text{Cl-O}}$	-0.24 eV	-0.27 eV	-0.22 eV
	$\Delta \mathcal{V}_e$	-0.20 V	-0.08 V	-0.05 V
Fig. 2c	$\Delta E_{\text{Cl-O}}$	+0.61 eV	+0.07 eV	+0.01 eV
	$\Delta \mathcal{V}_e$	-0.73 V	-0.33 V	-0.11 V

TABLE III: Energy cost ( $\Delta E_{\text{Cl-O}}$ ) of  $\text{Cl}^-$  insertion into uncharged  $\text{V}_\text{O}$  as a function of simulation cell size.  $\Delta \mathcal{V}_e$  is the computed voltage with the inserted  $\text{Cl}^-$  versus without; it is zero at infinite system size and is another measure of convergence.  $n \times m$  indicates supercell sizes as multiples of each baseline simulation cell. (\*) The  $\text{V}_\text{O}$  considered is at  $z=18.2 \text{ \AA}$ , not  $z=26.5 \text{ \AA}$  depicted in Fig. 5.

cells should make  $\Delta E_{\text{Cl-O}}$  even more favorable (Sec. II C), we have not considered larger cells once  $\Delta E_{\text{Cl-O}} < 0$ ; the qualitative conclusion that  $\text{Cl}^-$  insertion into  $\text{V}_\text{O}^{2+}$  is in general favorable would be unchanged.

LDOS plots for systems with  $\text{Cl}^-$  insertion (not shown) do not reveal states in the gap in the oxide region for either  $\text{V}_\text{O}$  or  $\text{V}_\text{O}^{2+}$ , suggesting that the  $\text{Cl}^-$  has driven the  $f$ -center orbital(s) associated with the  $\text{V}_\text{O}$  into the valence or conduction band. Bader charge analysis for  $\text{Cl}^-$  insertion into  $\text{V}_\text{O}$  yields expected results. Each  $\text{Cl}^-$  is found to carry  $\sim 8 e^-$ . So  $\text{Cl}^-$  is indeed a monovalent anion in the lattice, giving it a net  $\sim +|e|$  change in charge when substituting for an  $\text{O}^{2-}$  in the lattice. This induces a  $\sim -|e|$  net charge in the metal zone regardless of whether there is deprotonation in the system (Table IV).

### E. $\text{Cl}^- \rightarrow \text{OH}^-$ Substitution

Finally, for completeness, we consider Eq. 2 using the same  $\text{Cl}^-$   $\Delta G_{\text{hyd}}$  we have applied in this work. Eq. 2 is not an electrochemical process; no electron is exchanged with the metal. The  $\alpha\text{-Al}_2\text{O}_3$  (0001) reactant and product surface slabs used in the calculations have stoichiometries  $\text{Al}_{68}\text{O}_{54}\text{H}_6$  and  $\text{Al}_{68}\text{O}_{54}\text{H}_5\text{Cl}$  (Fig. 8), respectively. Eq. 2 is found to be endothermic by  $\Delta E=+1.54 \text{ eV}$  at standard state for both  $\text{Cl}^-$  and  $\text{OH}^-$  anions.

figure	deprot.	metal	oxide	water
Fig. 2a	0	-0.93	0.92	0.01
Fig. 2a	2	-0.75	0.88	0.12
Fig. 2b	0	-0.99	0.99	0.00
Fig. 2b	3	-1.10	1.11	-0.01
Fig. 2c	0	-0.85	0.84	0.01
Fig. 2c	2	-0.86	0.84	0.01

TABLE IV: Change in charge (in units of  $|e|$ ) due to  $\text{Cl}^-$  substitution for an  $\text{O}^{2-}$  in each zone ( $\Delta c(Z)$ ), counting both electrons and nuclei, relative to the slab without a  $\text{Cl}^-$ ; the number of H atoms removed from the surface is “deprot.” Unlike in Table II, the number of surface deprotonation is the same for the reference and the target slab.

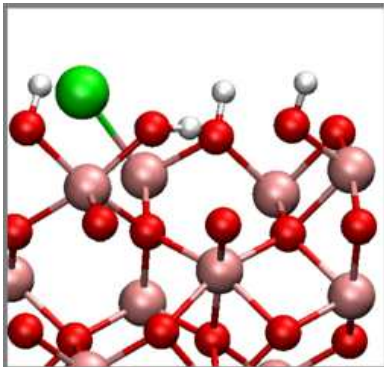


FIG. 8: Substituting a  $\text{Cl}^-$  for a surface  $\text{OH}^-$  group on the  $\alpha\text{-Al}_2\text{O}_3$  (0001) surface.

“Standard state” means that  $[\text{OH}^-]=1.0$  M, which is  $\text{pH}=14$ .  $\Delta E$  at lower  $\text{pH}$  can be estimated using the Nernst equation where each decade of  $\text{OH}^-$  product dilution reduces the endothermicity by 0.0592 eV. At  $\text{pH}=7$  or  $\text{pH}=0$ ,  $\Delta E$  is lowered to 1.12 eV and 0.71 eV, respectively. However, they remain energetically unfavorable. These findings dovetail with the geochemistry expectation that  $\text{Cl}^-$  does not react with surface  $\text{AlOH}$  groups at  $\text{Al}_2\text{O}_3/\text{water}$  interfaces. This prediction is qualitatively similar to that in Ref. 56 which applies a different DFT functional. Ref. 56 predicts that Cl substitution on the  $\text{Al}_2\text{O}_3$  (100) surface is favorable; we have not re-examined this possibility. DFT calculations have been applied to examine  $\text{Cl}^-$  substitution or insertion on other oxide surfaces,<sup>57–61</sup> but the  $\text{Cl}^-$  reference states are generally different from that applied in this work. Potential-of-mean-force simu-

lations for desorption of  $\text{Cl}^-$  from the surface in liquid water conditions may be applied to re-examine the desorption free energy in the future.<sup>103</sup>

#### IV. OUTLOOK

We emphasize the need to use DFT simulation cells with explicit metal/passivating oxide interfaces. Even though such calculations are costly, approximations are involved, and currently insufficient experimental input is available to pinpoint all structural/electronic interfacial properties, they can yield qualitatively new insights regarding electric fields, contact potentials, band-offsets, and charge-transfer effects which are not available in calculations without explicit metal/oxide interfaces. Our modeling work provides a renewed impetus for experimental characterization of metal/passivating oxide interfaces.

Computational voltage control, and correlation of predicted voltages with the onset associated with pitting, remain challenging. This is because the potential drop inside the oxide film ( $\Phi_f$ ), the contact potential at the metal/oxide film interface ( $\Phi_{mf}$ ), and the oxide/electrolyte interfacial contribution ( $\Phi_{fs}$ ) all add up to the single-valued applied voltage ( $\Phi_{ext}$ ). An overall charge-neutral oxide/electrolyte interface is predicted to yield only a global shift ( $\Phi_{fs}$ ) to the electronic band alignment, while changes in the metal/film interface yield large scale changes in the band structure. Future experimental work that isolates these separate contributions would be invaluable. Alternatively, the elucidation of the definitive atomic length-scale structure at the metal/oxide interface via cross-sectional imaging technique will enable more accurate DFT predictions of these quantities. DFT functional accuracy, simulation cell sizes, atomic length-scale interfacial structures, surface charges, oxide film thickness, and oxide phase specificity (including the possibility of amorphous oxides) all influence the predictions. Electric double layers in the aqueous electrolyte outside the oxide surface need to be explicitly included (say, via classical force field molecular dynamics simulations, or via the quantum continuum approach<sup>86</sup>), and added to the DFT work functions to afford quantitative comparisons with experiment voltages. The roles of salt and carbon dioxide on atmospheric corrosion should also be addressed in these models.<sup>105</sup> Despite these challenges, our work paves the way for further computational studies of the complex but crucial passivating oxide film interfaces relevant to corrosion phenomena.



## V. CONCLUSION

In this work, we examine the charges in oxygen vacancies ( $V_O$ ) inside crystalline  $Al_2O_3$  model surface films covering Al and Au (111) surfaces. Several models of metal/oxide interfaces, with and without grain boundaries, are considered. In all cases, when there is no electric field in the oxide film (“flat-band” configuration), we predict that  $V_O$  is charge-neutral. Creating negative surface charges by deprotonation of surface OH groups generates electric fields. These fields are needed to yield  $V_O^{2+}$  which are postulated to be crucial in the point defect model (PDM) widely used to analyze corrosion behavior.<sup>3</sup> The required potential gradients have slopes opposite to those typically seen in corrosion study schematics.<sup>3</sup>  $V_O^{2+}$  preferentially resides near the negatively charged oxide outer surfaces, while charge neutral  $V_O$  does not. Future DFT work along these lines for metals like Fe and Ni, which are more electropositive than Al and should support  $V_O^{2+}$  more readily, may be of significant interest, although Fe(III) ions in  $Fe_2O_3$  oxide films may undergo redox changes and complicate the analysis.

$Cl^-$  is predicted to be energetically favorable when inserted into some  $V_O$  or  $V_O^{2+}$ , depending on the oxide structure, existence of grain boundary, and applied voltage. In contrast,  $Cl^-$  substitution of  $OH^-$  groups coordinated to surface Al cations does not depend on voltage and is predicted to be energetically unfavorable on flat  $\alpha-Al_2O_3$  (0001) surfaces. Such substitutions have been inferred in analysis of EXAFS studies;<sup>13</sup> they may occur on other crystal facets,<sup>56</sup> in oxide pores, or on amorphous oxide surfaces.

### Appendix: Structure/voltage relation at different interfaces

In this appendix, we seek to isolate the effects of the metal-film interface and of the film-solvent interface using a combinatorial approach. We focus on the Al (111)/ $\alpha-Al_2O_3$  (0001) system. No oxide-surface  $H^+$  vacancy,  $V_O$ , or  $Cl^-$  insertion is considered in this appendix, which allows us to use smaller simulation cells. A surface unit cell of lateral dimension  $4.81 \times 8.33 \text{ \AA}^2$  is applied in all cases. This is a “doubled” surface cell in the sense that it has twice the lateral area of the normal  $\alpha-Al_2O_3$  (0001) surface cell.

Two interfacial structures at the Al/oxide interface, with and without AIMD pre-equilibration for 1.5 ps before optimizing the atomic configurations, are shown in Fig. 9a-b.

Both start with the “FCC” metal/oxide alignment,<sup>29</sup> and are created by adding a Al below each undercoordinated O-anion on the  $\alpha$ -Al<sub>2</sub>O<sub>3</sub> (0001) inner surface (Fig. 9b). Upon applying AIMD (Fig. 9a), three of the six Al atoms per doubled surface unit cell thus added are transferred on to the Al metal region, and the other three remain bonded to O-anions. This Al-O bonding configuration is similar with that in Ref. 24; it is slightly different from the optimized configuration using an undoubled surface unit cell where the equivalent of 4 surface O atoms would remain bonded to Al below.<sup>29</sup> The AIMD equilibration lowers the total energy of the simulation cell, by  $\sim 1.7$  eV.

Two possible interfacial structures at the oxide surface, with 2- and 3-adsorbed H<sub>2</sub>O molecules per exposed surface Al<sup>3+</sup>, are depicted in Fig. 9c-d. Our previous work,<sup>46</sup> and the current Fig. 2c, have 2 H<sub>2</sub>O per surface Al<sup>3+</sup>, while Fig. 2a has 3 H<sub>2</sub>O per surface Al<sup>3+</sup>. With these two sets of interfaces, we create three slab configurations: (I) Fig. 9a & Fig. 9c; (II) Fig. 9a & Fig. 9d (which is effectively Fig. 2a); (III) Fig. 9b & Fig. 9d. See Table V.

The corresponding local densities of state and electrostatic potential along the  $z$ -direction of these three slabs, after optimization of atomic coordinates, are depicted in Fig. 10a-c and Fig. 10d-f, respectively. The overall  $\mathcal{V}_e$  are -0.05 V, -1.98 V, and -2.69 V vs. SHE for systems (I)-(III), respectively. This suggests that both interfaces affect the overall voltage but the oxide-solvent interface can be dominant. Comparing (II) and (III), the AIMD-equilibrated structure contains fewer Al<sup>δ+</sup>-O bonds at the metal/oxide, which is correlated with a smaller overall dipole moment and a more positive voltage via Eq. 6. The variation in  $\mathcal{V}_e$  is larger than in Ref. 24 because the Fig. 9b is metastable by a significant amount of energy.

Fig. 10 depicts local densities of states (LDOS) and integrated electrostatic potentials along the  $z$ -direction ( $V(z)$ ). They highlight how different interfaces affect local LDOS features. Systems (I) and (II) exhibit similar LDOS and  $V(z)$ , except at the oxide-“solvent” interface at  $z \sim 40$  Å, (the water zone) and except that the LDOS are globally shifted from each other by  $\sim 2$  eV. For example, The offsets between the oxide zone VBE and the Fermi level (i.e.,  $\Delta E_{\text{FVBE}}$ ) are  $\sim 2.88$  eV in both in both (I) and (II). These systems have the same metal-film interface, and the global shift must be due to the film-solvent interface (Table V). In contrast, systems (II) and (III) differ structurally only at the metal-film interface. There are substantial differences in the LDOS and  $V(z)$  between these systems. For example,  $\Delta E_{\text{FVBE}}$  now rises to 3.60 eV in (III) compared to 2.88 eV in (I) and (II). However, as expected, the LDOS near the film-solvent interfaces (the water zone) are very similar (but

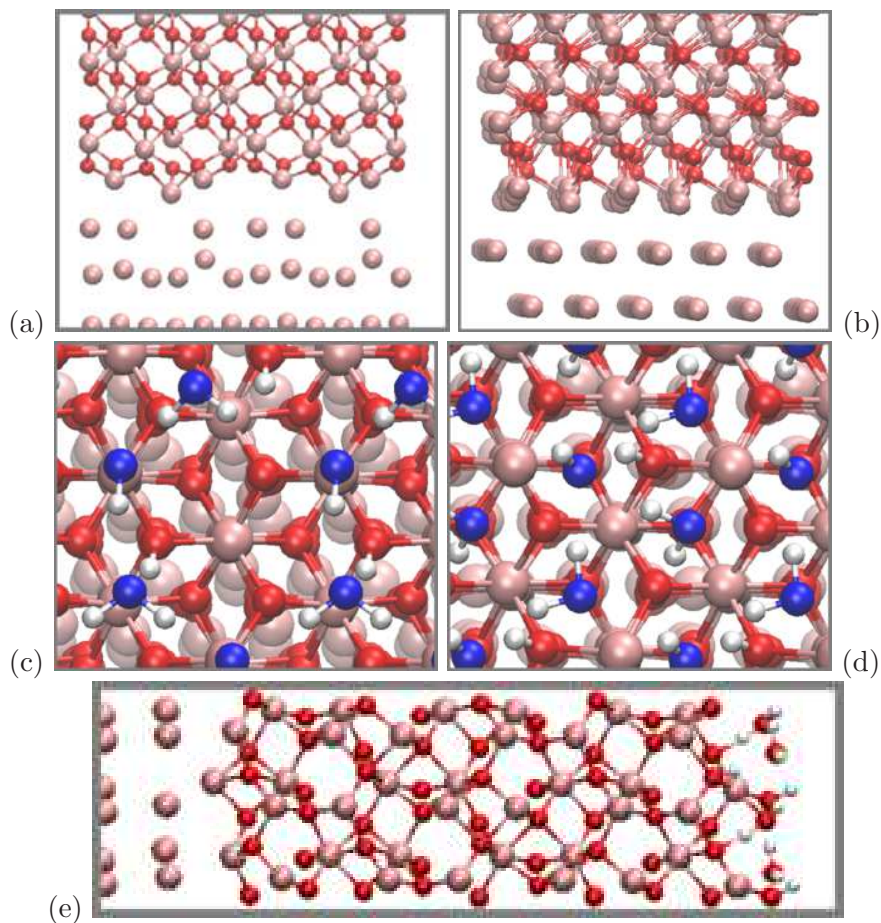


FIG. 9: (a)-(b) Close-up views of two possible Al/ $\alpha$ -Al<sub>2</sub>O<sub>3</sub> (0001) with and without AIMD pre-equilibration respectively. (c)-(d) Close-up views of two possible  $\alpha$ -Al<sub>2</sub>O<sub>3</sub> (0001) surfaces, with 2 or 3 adsorbed H<sub>2</sub>O per exposed surface Al<sup>3+</sup> cations. Some of these H<sub>2</sub>O are dissociated. (e) Simulation cell with a different number of Al atoms at the Al-metal side of the Al/Al<sub>2</sub>O<sub>3</sub> interface. The  $\alpha$ -Al<sub>2</sub>O<sub>3</sub> (0001)|H<sub>2</sub>O surface in Fig. 9e in fact resembles that of Fig. 9d.

slightly shifted in the  $z$  direction because of structural changes at the metal/oxide interface).

The system (II), with the AIMD-equilibrated Al (001)| $\alpha$ -Al<sub>2</sub>O<sub>3</sub> (0001) interface depicted in Fig. 9d, appears similar to that in Ref. 24. To further check the results of variations in the number of Al atoms in the top layer of the metal region per doubled surface cell, we have created yet another Al|Al<sub>2</sub>O<sub>3</sub> interfacial simulation cell with 5 rather than 3 Al atoms on the top metal layer per doubled cell and the outer oxide surface structure of Fig. 9d. The entire system is depicted in Fig. 9e. This alternative configuration (“alt” in Table V) yields a  $\mathcal{V}_e$  within 0.26 V of that of system (II). The offsets between the oxide zone VBE and the Fermi level ( $\Delta E_{\text{FVBE}}$ ) are 2.64 eV and 2.88 eV in the two cases, within 0.24 eV of

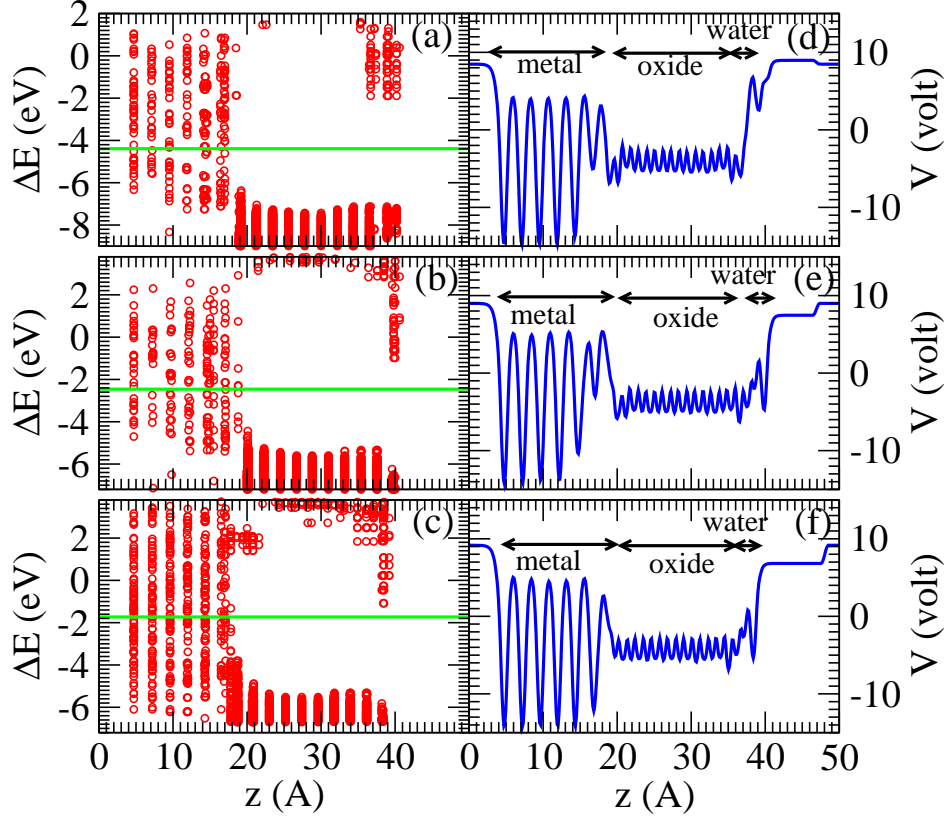


FIG. 10: (a)-(c) Localized densities of state for systems (I)-(III), respectively. (d)-(f) Electrostatic potentials for systems (I)-(III), respectively. The green lines denote Fermi levels, and vacuum is at  $\Delta E=0.0$  eV.

system	m f	f s	$\mathcal{V}_e$	$\Delta E_{\text{FVBE}}$
(I)	Fig. 9a	Fig. 9c	-0.02 V	2.64 eV
(II)	Fig. 9a	Fig. 9d	-1.98 V	2.88 eV
(III)	Fig. 9b	Fig. 9d	-2.69 V	3.59 eV
alt	Fig. 9e	Fig. 9e	-1.72 V	2.64 eV

TABLE V: Attributes of systems (I)-(III) examined in the appendix. Voltages are referenced to SHE. For the f|s interface, Fig. 9e and Fig. 9d are identical.

each other.

From the above analysis, we make the following observations about the metal/oxide and the oxide/vacuum interfaces. (i) The metal/oxide interface qualitatively modifies the orbital alignment across the oxide film. (ii) Varying the number of partially charged  $\text{Al}^\delta$  coordinated to the bottom layer of oxide at the metal/oxide interface has the most significant effect on the orbital alignment inside the oxide. (iii) Varying the number of Al atoms at the top layer of the metal surface at the interface, not coordinated to O-atoms in the oxide, has smaller effects on the band structure because such Al atoms are metallic and mostly uncharged, and do not give rise to large dipole moment changes that modify the band alignment. (iv) The structure of the oxide film outer surface has a significant effect on the overall work function and  $\mathcal{V}_e$ . However, its effect is to exert a global shift in the band structure and does not strongly affect the orbital alignment inside the oxide film – unless this interface is charged (e.g., via creating proton vacancies).

Finally, as discussed in Sec. II A, the interface between Al(111) and  $\alpha\text{-Al}_2\text{O}_3$  with a grain boundary is too large for us to perform AIMD pre-equilibration simulations. Instead, we displace the metal and oxide slabs in the  $x$ - and  $y$ - directions for a total of 13 cases. We find that  $\mathcal{V}_e$  averages to  $-1.47 \pm 0.03$  V, in good agreement with the  $-1.54$  V for the configuration considered in the main text. The simulation cell total energies exhibit a standard deviation  $0.04$  eV/nm<sup>2</sup> in the  $1.29$  nm<sup>2</sup> lateral surface area simulation cell; the LDOS are qualitatively similar. Hence we conclude that the lateral registry of the metal and oxide slabs does not strongly affect the LDOS in this system.

### Acknowledgement

We thank Nancy Missert, Peter Schultz, Quinn Campbell, and Katherine Jungjohann for useful suggestions. This work is funded by the Advanced Strategic Computing (ASC) Program. Sandia National Laboratories is a multi-mission laboratory managed and operated by National Technology and Engineering Solutions of Sandia, LLC, a wholly owned subsidiary of Honeywell International, Inc., for the U.S. Department of Energy’s National Nuclear Security Administration under contract DE-NA0003525. This paper describes objective technical results and analysis. Any subjective views or opinions that might be expressed in the document do not necessarily represent the views of the U.S. Department of Energy or

the United States Government.

---

- <sup>1</sup> R.W. Revie (eds) *Uhlig's Corrosion Handbook*, Third Edition. (Wiley, 2011)
- <sup>2</sup> J. Evertsson, F. Bertram, F. Zhang, L. Rullik, L.R. Merte, M. Shipilin, M. Soldemo, S. Ahmadi, N. Vinogradov, F. Carla, J. Weissenrieder, M. öthelid, J. Pan, A. Mikkelsen, J.-O. Nilsson, and E. Lundgren, *Appl. Sur. Sci.* **349**, 826-832 (2015).
- <sup>3</sup> C.Y. Chao, L.F. Lin, and D.D. Macdonald, *J. Electrochem. Soc.* **128**, 1187-1194 (1981).
- <sup>4</sup> L.F. Lin, C.Y. Chao, and D.D. Macdonald, *J. Electrochem. Soc.* **128**, 1194-1198 (1981).
- <sup>5</sup> D.D. Macdonald and X. Lei. *J. Electrochem. Soc.*, **163** C738-C744 (2016).
- <sup>6</sup> S. Sharifi-Asl, F. Mao, P. Lu, B. Kursten, and D.D. Macdonald. *Corrosion Sci.* **98**, 708-715 (2015).
- <sup>7</sup> P. Lu, R. Engelhardt, B. Kursten, and D.D. Macdonald. *J. Electrochem. Soc.* **163** C156-C163 (2016).
- <sup>8</sup> M. Liu, Y. Jin, C. Leygraf, and J. Pan. *J. Electrochem. Soc.* **166** C3124-C3130 (2019).
- <sup>9</sup> G. Engelhardt and D.D. Macdonald, *Corrosion Science* **46**, 2755-2780 (2004).
- <sup>10</sup> G.S. Frankel, *J. Electrochem. Soc.* **145**, 2186-2198 (1998).
- <sup>11</sup> C.J. Boxley, J.J. Watkins, and H.S. White, *Electrochem. Solid-State Lett.* **6**, B38-B41 (2003).
- <sup>12</sup> P.M. Natishan and W.E. O'Grady. *J. Electrochem. Soc.*, **161**, C421-C432 (2014).
- <sup>13</sup> P.M. Natishan, *Corrosion* **74**, 263-275 (2018).
- <sup>14</sup> S.Y. Yu, W.E. O'Grady, D.E. Ramaker, and P.M. Natishan, *J. Electrochem. Soc.* **147**, 2952-2958 (2000).
- <sup>15</sup> E. McCafferty, *Corrosion Science* **45**, 1421-1438 (2003).
- <sup>16</sup> V. Maurice and P. Marcus. *Electrochim. Acta* **84**, 129-138 (2012).
- <sup>17</sup> N.J. Laycock, M.H. Moayed, and R.C. Newman, *J. Electrochem. Soc.* **145**, 2622-2628 (1998).
- <sup>18</sup> C. Punckt, M. Bölscher, H.H. Rotermund, A.S. Mikhailov, L. Organ, N. Budiansky, J.R. Scully, and J.L. Hudson, *Science* **305**, 1133-1136 (2004).
- <sup>19</sup> J.B. Bessone, D.R. Salinas, C.E. Mayer, M.E. Ebert, and W.J. Lorenz, *Electrochim. Acta* **37**, 2283-2290 (1992).
- <sup>20</sup> G.A. DiBari and H.J. Read, *Corrosion* **27**, 483-494 (1971).
- <sup>21</sup> L.M. Serna, K R. Zavadil, C.M. Johnson, F.D. Wall, and J.C. Barbour, *J. Electrochem. Soc.*,

- 153**, B289-B295 (2006).
- <sup>22</sup> F. Brown and W.D. Mackintosh, *J. Electrochem. Soc.*, **120** 1096-1102 (1973).
- <sup>23</sup> K. Shimizu, G.M. Brown, K. Kobayashi, P. Skeldon, G.E. Thompson, and G.C. Wood, *Corrosion Sci.* **41**, 1835-1847 (1999).
- <sup>24</sup> E.-G. Kim and J.-L. Bredas, *Organic Electronics*, **14**, 569-574 (2013).
- <sup>25</sup> I.G. Batyrev and L. Kleinman, *Phys. Rev. B* **64**, 033410 (2001).
- <sup>26</sup> G. Pilania, B.J. Thijssen, R.G. Hoagland, I. Lazic, S.M. Valone, and X.-Y. Liu, *Sci. Rep.* **4**, 4485 (2014).
- <sup>27</sup> M. Koberidze, M.J. Puska, and R.M. Nieminen, *Phys. Rev. B* **97**, 195406 (2018).
- <sup>28</sup> W. Zhang and J.R. Smith, *Phys. Rev. Lett.* **85**, 3225-3228 (2000).
- <sup>29</sup> D.J. Siegel, L.G. Hector, and J.B. Adams, *Phys. Rev. B* **65**, 085415 (2002).
- <sup>30</sup> X.-G. Wang, J.R. Smith, and A. Evans, *Phys. Rev. Lett.*, **89**. 286102 (2002).
- <sup>31</sup> Y. Liu and X.-S. Ning, *Comput. Mater. Sci.* **85**, 193-199 (2014).
- <sup>32</sup> S.V. Eremeev, S. Schmauder, S. Hocker, and S.E. Kulkova, *Physica B* **404**, 2065-2071 (2009).
- <sup>33</sup> D. Costa, T. Ribeiro, F. Mercuri, G. Pacchioni, and P. Marcus. *Adv. Mater. Interfaces* **1**, 1300072 (2014).
- <sup>34</sup> S. Surendralal, M. Todorova, M.W. Finnis, and J. Neugebauer, *Phys. Rev. Lett.* **120**, 246801 (2018).
- <sup>35</sup> C.-H. Zhang, B. Chen, Y. Jin, and D.-B. Sun, *J. Phys. Chem. Solids* **110**, 129-135 (2017).
- <sup>36</sup> X.-X. Yu, A. Gulec, K.L. Cwalina, J.R. Scully, and L.D. Marks. *Corrosion*, **75**, 616-627 (2019).
- <sup>37</sup> X.-X. Yu and L.D. Marks, *Corrosion*, **75**, 152-166 (2019).
- <sup>38</sup> J.R. Weber, A. Janotti, and C.G. Van de Walle. *Microelectronic Engineering* **86** 1756-1759 (2009).
- <sup>39</sup> M. Choi, A. Janotti, and C.G. Van de Walle. *J. Appl. Phys.* **113**, 044501 (2013).
- <sup>40</sup> F. Janetzko, R.A. Evarestov, T. Bredow, and K. Jug, *Phys. Stat. Sol. B* **241**, 1032-1040 (2004).
- <sup>41</sup> J. Carrasco, J.R.B. Gomes, and F. Illas. *Phys. Rev. B* **69**, 064116 (2004).
- <sup>42</sup> J. Carrasco, N. Lopez, and F. Illas. *Phys. Rev. Lett.* **93**, 225502 (2004).
- <sup>43</sup> N.D.M. Hine, K. Frensch, W.M.C. Foulkes, and M.W. Finnis, *Phys. Rev. B* **79**, 024112 (2009).
- <sup>44</sup> J. Bonini, D. Vanderbilt, and R.M. Rabe, *Phys. Rev. B* **102**, 045141 (2020).
- <sup>45</sup> Q. Campbell and I. Dabo, *Phys. Rev. B*, **96**, 205308 (2017).
- <sup>46</sup> K. Leung, *Phys. Chem. Chem. Phys.* **22**, 10412-10425 (2020).

- <sup>47</sup> P. Cornette, D. Costa, and P. Marcus, *J. Electrochem. Soc.* **167**, 161501 (2020).
- <sup>48</sup> J. Strand, M. Kaviani, D. Gao, A. El-Sayed, V.V. Afanas'ev, and A.L. Shluger. *J. Phys.: Condens. Matter*, **30**, 233001 (2018).
- <sup>49</sup> O.A. Dicks, J. Cottom, A.L. Shluger, and V.V. Afanas'ev. *Nanotechnology* **30**, 205201 (2019).
- <sup>50</sup> H. Yu, C. Chen, R. Jiang, P. Qiu, and Y. Li. *J. Phys. Chem. C* **116**, 25478-25485 (2012).
- <sup>51</sup> P.M. Natishan, W.E. O'Grady, E. McCafferty, D.E. Ramaker, K. Pandya, and A. Russell. *J. Electrochem. Society*, **146**, 1737-1740 (1999).
- <sup>52</sup> P.M. Natishan, S.Y. Yu, W.E. O'Grady and D.E. Ramaker. *Electrochim. Acta* **47**, 3131-3136 (2002).
- <sup>53</sup> W.E. O'Grady, D.F. Roeper, and P.M. Natishan. *J. Phys. Chem. C* **115**, 25298-25303, (2011).
- <sup>54</sup> Z. Wang, A. Seyeux, S. Zanna, V. Maurice, and P. Marcus. *Electrochim. Acta* **329**, 135159 (2020).
- <sup>55</sup> J. Wirth, J. Schacht, P. Saalfrank, and B. Paulus. *J. Phys. Chem. C* **120**, 9713-9718 (2016).
- <sup>56</sup> L. Marks, *Corrosion*, **74**, 295-311 (2017).
- <sup>57</sup> A. Bouzoubaa, B. Diawara, V. Maurice, C. Minot, and P. Marcus, *Corros. Sci.* **51**, 941-948 (2009).
- <sup>58</sup> K.O. Sarfo, P. Murkute, O.B. Isgor, Y. Zhang, J. Tucker, and L. Arnadottir, *J. Electrochem. Soc.* **167**, 121508 (2020).
- <sup>59</sup> K.N. Nigussa, K.L. Bielsen, O. Borck, and J.A. Stovneng, *Corros. Sci.* **53**, 3612-3622 (2011).
- <sup>60</sup> Q. Pang, H. DorMohammadi, O.B. Isgor, and L. Arnadottir, *Corrosion*, **76**, 690-697 (2020).
- <sup>61</sup> Q. Pang, H. DorMohammadi, O.B. Isgor, and L. Arnadottir, *Corros. Sci.*, **154**, 61-69 (2019).
- <sup>62</sup> A. Kolics, J.C. Polkinghorne, A.E. Thomas, and A. Wieckowski. *Chem. Mater.* **10**, 812-824 (1998).
- <sup>63</sup> A. Kolics, J.C. Polkinghorne, and A. Wieckowski. *Electrochim. Acta* **43**, 2605-2618 (1998).
- <sup>64</sup> M. Dietzel and G. Böhme. *Geochim. Cosmochim. Acta*, **69**, 1199-1211 (2005).
- <sup>65</sup> M. Aykol and K.A. Persson, *ACS Appl. Mater. Interfaces* **10**, 3039-3045 (2018).
- <sup>66</sup> Y.Y. Cheng, S.X. Lu, W.G. Xu, and H.D. Wen, *RSC Adv.* **5**, 15387-15394 (2015).
- <sup>67</sup> D. Costa, T. Ribeiro, P. Cornette, and P. Marcus. *J. Phys. Chem. C*, **120**, 28607-28616 (2016).
- <sup>68</sup> C.D. Taylor, A. Chandra, J. Vera, and N. Sridhar, *J. Electrochem. Soc.*, **162**, C347-C353 (2015).
- <sup>69</sup> L.J. Criscenti, R.T. Cygan, A.S. Kooser, and H.K. Moffat. *Chem. Mater.* **20**, 4682-4693 (2008).



- <sup>70</sup> B.F. Ngouana-Wakou, P. Cornette, M.C. Valero, D. Costa and P. Raybaud, *J. Phys. Chem. C* 2017, **121**, 10351-10363.
- <sup>71</sup> M.C. Valero, B. Prelot and G. Leferve, *Langmuir* 2019, **35**, 12986-12992.
- <sup>72</sup> M. DelloStritto, S.M. Piontek, M.L. Klein and E. Borguet, *J. Phys. Chem. C* 2018, **122**, 21284-21294.
- <sup>73</sup> R. Wang, M. DelloStritto, R.C. Remsing, V.Carnevale, M.L. Klein and E. Borguet, *J. Phys. Chem. C* 2019, **123**, 15618-15628.
- <sup>74</sup> G. Kresse and J. Furthmüller, *Phys. Rev. B*, **54**, 11169 (1996).
- <sup>75</sup> G. Kresse and J. Furthmüller, *Comput. Mater. Sci.*, **6**, 15-50 (1996).
- <sup>76</sup> G. Kresse and D. Joubert, *Phys. Rev. B*, **59**, 1758-1775 (1999).
- <sup>77</sup> J. Paier, M. Marsman, and G. Kresse, *J. Chem. Phys.*, **127**, 024103 (2007).
- <sup>78</sup> J.P. Perdew, K. Burke, and M. Ernzerhof, *Phys. Rev. Lett.*, **77**, 3865-3868 (1996).
- <sup>79</sup> J. Heyd, G.E. Scuseria, and M. Ernzerhof, *J. Chem. Phys.*, **118**, 8207-8215 (2003).
- <sup>80</sup> J. Heyd, G.E. Scuseria, and M. Ernzerhof, *J. Chem. Phys.*, **124**, 219906 (2006).
- <sup>81</sup> O.A. Vydrov, J. Heyd, A.V. Kruckau, and G.E. Scuseria, *J. Chem. Phys.*, **125**, 074106 (2006).
- <sup>82</sup> Y. Lei, Y. Gong, Z. Duan, and G. Wang, *Phys. Rev. B* **87**, 214105 (2013).
- <sup>83</sup> T. Sritharan, Y.B. Li, C. Xu, and S. Zhang, *J. Mater. Res.* **23**, 1371-1382 (2008).
- <sup>84</sup> C. Xu, T. Sritharan, S.G. Mhaisalkar, M. Srinivasan, and S. Zhang, *Appl. Sur. Sci.* **253**, 6217-6221 (2007).
- <sup>85</sup> H.P. Pinto, R.M. Nieminen, and S.D. Elliott. *Phys. Rev. B* **70**, 125402 (2004).
- <sup>86</sup> Q. Campbell and I. Dabo, *J. Chem. Phys.* **151**, 044109 (2019).
- <sup>87</sup> K. Leung, S.B. Rempe, O.A. von Lilienfeld, *J Chem. Phys.*, **130**, 204507 (2009).
- <sup>88</sup> K.J. McCallum and J.E. Mayer, *J. Chem. Phys.* **11**, 56-63 (1943).
- <sup>89</sup> C.-G. Zhan and D.A. Dixon, *J. Phys. Chem.* **106**, 9737-9744 (2002).
- <sup>90</sup> G. Henkelman, A. Arnaldsson, and H. Jónsson, *Comput. Mater. Sci.* **36**, 354-360 (2006).
- <sup>91</sup> S. Trasatti, *J. Electroanal. Chem.* **209**, 417-428 (1986).
- <sup>92</sup> H. Musada, N. Ishida, Y. Ogata, D. Ito, and D. Fujita, *Nanoscale*, **9**, 893-898 (2017).
- <sup>93</sup> M. Todorova and J. Neugebauer, *Phys. Rev. Appl.*, **1**, 014001 (2014).
- <sup>94</sup> C.D. Taylor, S.A. Wasileski, J.-S. Filhol, and M. Neurock, *Phys. Rev. B*, **73**, 165402 (2006).
- <sup>95</sup> M. Otani, I. Hamada, O. Sugino, Y. Morikawa, Y. Okamoto, and T. Ikeshoji, *J. Phys. Soc. Jpn.*, **77**, 024802 (2008).

- <sup>96</sup> K. Leung and C.M. Tenney, *J. Phys. Chem. C*, **117**, 24224-24235 (2013).
- <sup>97</sup> K. Leung, *Phys. Chem. Chem. Phys.* **17**, 1637-1643 (2015).
- <sup>98</sup> K. Letchworth-Weaver and T.A. Arias, *Phys. Rev. B*, **86**, 075140 (2012).
- <sup>99</sup> J. Haruyama, T. Ikeshoji, and M. Otani, *Phys. Rev. Mater.*, **2**, 095801 (2018).
- <sup>100</sup> N. Bonnet, T. Morishita, O. Sugino, and M. Otani, *Phys. Rev. Lett.*, **109**, 266101 (2012).
- <sup>101</sup> I. Hamada, O. Sugino, N. Bonnet, and M. Otani, *Phys. Rev. B*, **88**, 155427 (2013).
- <sup>102</sup> J. Neugebauer and M. Scheffler, *Phys. Rev. B*, **46**, 16067-16080 (1992).
- <sup>103</sup> K. Leung, L.J. Criscenti, A.W. Knight, A.G. Ilgen, T.A. Ho, and J.A. Greathouse, *J. Phys. Chem. Lett.*, **9**, 5379-5385 (2018).
- <sup>104</sup> P.A. Schultz, *Phys. Rev. Lett.* **96**, 246401 (2006).
- <sup>105</sup> R.F. Schaller, C.F. Jove-Colon, J.M. Taylor, and E.J. Schindelhotz, *NPJ Materials Degradation* **1**, 20 (2017).